

Charged-particle multiplicities associated with large-transverse-momentum photons*

R. Kephart, G. Finocchiaro, P. Grannis, D. Green,[†] H. Jöstlein, D. Lloyd Owen, and R. Thun[‡]
State University of New York, Stony Brook, New York

G. Bellettini,[§] P. L. Braccini, R. Castaldi,^{||} V. Cavalinni, T. Del Prete, P. Laurelli, G. Sanguinetti, and M. Valdata
Istituto Nazionale di Fisica Nucleare, Sezione di Pisa, Italy
and Istituto di Fisica dell'Università, Pisa, Italy

(Received 21 May 1976)

We have measured the charged-particle multiplicities of events containing a large-transverse-momentum (p_{\perp}) photon produced near center-of-mass polar angles (θ) of 90° , 17.5° , and 8° in proton-proton collisions. The data were obtained at the CERN Intersecting Storage Rings at center-of-mass energies of 23, 31, 45, 53, and 62 GeV and for the transverse-momentum range $0 \leq p_{\perp} \leq 4.5$ GeV/ c . When the photons are detected near $\theta = 90^\circ$, the associated multiplicity in the hemisphere away from the observed photon is found to increase with increasing photon transverse momentum. In the hemisphere containing the photon, the associated multiplicity decreases at the lowest energy and is approximately constant at the highest energies. The data at $\theta = 17.5^\circ$ and 8° are similar, with the exception that the particle multiplicities near the detected photon are found to decrease with increasing photon p_{\perp} at all energies. No strong back-to-back structure is observed in the data; however, as the photon emission angle is changed, some shift of the multiplicity distributions in the direction opposite the photon is observed. The data at all three polar angles show a broad peak in the azimuthal angular distributions at $\phi = 180^\circ$ (opposite the detected photon). Finally, the data are compared to a simplified picture for particle production in high- p_{\perp} events, and to the various classes of high- p_{\perp} models that have been proposed.

I. INTRODUCTION

In the past four years there has been considerable interest in the characteristics of events in which large-transverse-momentum hadrons are produced in high-energy hadron collisions. The presence of more large- p_{\perp} hadrons than expected from an extrapolation of single-particle cross sections at low p_{\perp} (see Ref. 1) gives rise to the feeling that a new component or aspect of hadronic forces is being seen. The emergence, at large p_{\perp} , of a power-law behavior in p_{\perp} has motivated attempts to unify the description of short-distance hadronic structure as probed in hadron-hadron and lepton-hadron collisions.

Various phenomenological explanations² have been given for the large- p_{\perp} cross sections; in particular, models in which hadron constituents undergo large-angle collisions have been extensively explored. There are also less detailed models in which the large- p_{\perp} phenomena are interpreted in terms of cluster or fireball production in the primary hadron collision; decay products of these objects include the observed hadrons at large p_{\perp} .

In order to sharpen our understanding of the production mechanism, more detailed information on the structure of events containing a large- p_{\perp} hadron is desirable. In particular, it is of interest to know what other particles are produced in association with the large- p_{\perp} particle. We would like to know how the multiplicity, angular distributions,

and momentum distributions of the other particles in the event depend on the properties of the large- p_{\perp} hadron.

The present work reports an extensive series of measurements of the associated multiplicity and angular distribution of charged hadrons produced in events containing large- p_{\perp} photons. These photons arise predominantly from π^0 decays. The measurements were performed at the CERN Intersecting Storage Rings (ISR) at c.m. energies of $\sqrt{s} = 23, 31, 45, 53, \text{ and } 62$ GeV. The experiment employed a large solid-angle coverage of scintillator hodoscopes to record the charged particles. The photons were detected by an array of lead-glass Čerenkov counters and associated scintillators. Data were taken for the photon detector centered at three c.m. angles: $\theta = 90^\circ, 17.5^\circ, \text{ and } 8^\circ$.

Preliminary results on the 90° data at $\sqrt{s} = 53$ GeV from this experiment have been published previously.³ Some aspects of the s dependence and the θ dependence observed in this experiment have also been discussed.⁴ Other experiments⁵ have studied various aspects of the structure of events with a large- p_{\perp} secondary, including information on multiplicities, angular dependences, and momentum correlations. Preliminary analysis of the single-photon inclusive cross sections from this experiment shows reasonable agreement with the published data at $\theta = 90^\circ$.¹ A more complete analysis of the single-photon spectra and their angle and energy dependences is in progress.

This paper is organized as follows: In Sec. II

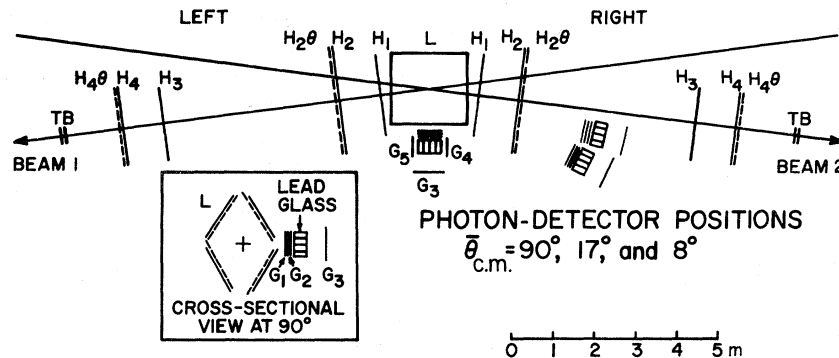


FIG. 1. Layout of the apparatus. H_1 , H_2 , H_3 , H_4 , and TB are trigger hodoscopes. $H_2\theta$, $H_4\theta$, and L measure multiplicities. The photon detector is shown at each of the positions used for data taking. The inset shows the photon detector and hodoscope L arrangement as seen along the beam bisector.

we describe the experimental apparatus and the calibration procedures used for the photon detector.⁶ Section III discusses the event-selection criteria and the data analysis. Results are presented in Sec. IV. Section V is devoted to a phenomenological discussion of these results, in which the evidence for distinct mechanisms of particle production is examined. Finally, in Sec. VI, we confront various phenomenological models with the data of this and other experiments.

II. EXPERIMENTAL APPARATUS

This experiment was performed at the CERN ISR using colliding proton beams of 11.7, 15.4, 22.4, 26.6, and 31.4 GeV/ c . During the period of the experiment, typical luminosities were of the order $10^{30} \text{ cm}^{-2} \text{ sec}^{-1}$. The beam momentum spread was typically $\leq 2\%$.

The experimental apparatus was a slightly modified version of that used to measure the p - p total cross section at the ISR.⁷ It consisted of a large array of scintillation-counter hodoscopes, covering about 80% of the full solid angle, and a photon detector. The photon detector was positioned at three different locations during the course of the experiment. These locations corresponded to the c.m. angles of 90° , 17.5° , and 8° . Figure 1 shows the layout of the hodoscopes and photon detector at the three angular settings. Table I gives the locations of the photon detector.

The hodoscope system has been described in detail elsewhere.⁷ Here we note only its general properties. Hodoscopes H_1 , H_2 , H_3 , and H_4 each contained a plane of eight counters, surrounding the exiting beam pipes to the left and right of the intersection point. The TB's were small hodoscopes covering the smallest scattering angles accessible. The above counters were used solely for the triggering of the system. In addition, there

were finely divided hodoscopes $H_2\theta$ and $H_4\theta$ around both beams, and the hodoscope L in the central region. The $H_2\theta$ hodoscopes were divided into ten rings in polar angle θ and further subdivided into quadrants or octants of azimuthal angle ϕ . The $H_4\theta$ were divided similarly in the azimuthal angle, but into 14 rings in θ . The L hodoscope, shown in the inset of Fig. 1, was divided into four azimuthal planes. Each such plane had one layer with seven θ subdivisions and another layer with five ϕ subdivisions. All information presented here on multiplicity and angular distributions was obtained from $H_2\theta$, $H_4\theta$, and L .

The photon detector consisted of a 4×4 array of lead-glass total absorption Čerenkov counters along with ancillary scintillation-counter hodoscopes used for triggering purposes and background rejection. An exploded view of the detector is shown in Fig. 2. Each of these counters was made up of a $15 \times 15 \times 35$ -cm block of lead-glass, the depth corresponding to 14.6 radiation lengths.

TABLE I. Photon-detector positions.

Position I	$\theta_{\max} = 104^\circ$ $\eta = -0.25$ $\theta_{\text{mean}} = 90.0^\circ$ $\eta = 0$ $\theta_{\min} = 76.0^\circ$ $\eta = 0.25$ $\Delta\phi = \pm 14^\circ$
	Laboratory solid angle = 0.30 sr
Position II	$\theta_{\max} = 21.9^\circ$ $\eta = 1.64$ $\theta_{\text{mean}} = 17.5^\circ$ $\eta = 1.87$ $\theta_{\min} = 13.4^\circ$ $\eta = 2.14$ $\Delta\phi = \pm 14^\circ$
	Laboratory solid angle = 0.022 sr
Position III	$\theta_{\max} = 12.6^\circ$ $\eta = 2.20$ $\theta_{\text{mean}} = 7.94^\circ$ $\eta = 2.67$ $\theta_{\min} = 3.81^\circ$ $\eta = 3.40$ $\Delta\phi = \pm 27.5^\circ$
	Laboratory solid angle = 0.021 sr

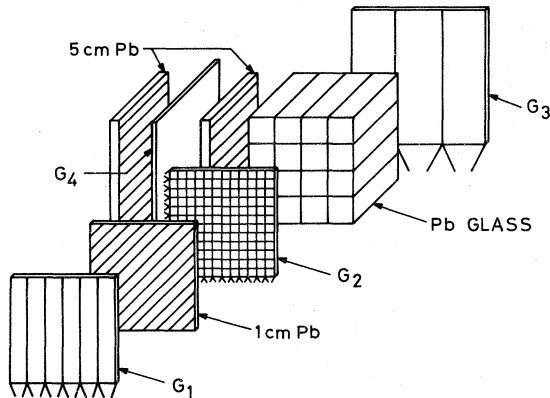


FIG. 2. Exploded view of the photon detector. G_1 , G_2 , and G_3 are scintillator hodoscopes. Photons from the beam intersection are normally incident on G_1 . Counter G_5 (not shown) is on the opposite side of the lead-glass array to G_4 .

The counters were optically isolated from each other and had provisions for mounting two light-emitting diodes and a radioactive source used for energy calibration purposes. The photon energy was determined from a measurement of the total pulse area of the signals from the 16 lead-glass Čerenkov counters.

Between the lead-glass Čerenkov counters and the intersection region were two scintillation-counter hodoscopes G_1 and G_2 , separated by a 1-cm lead converter (1.8 radiation lengths). Hodoscope G_1 consisted of six vertical counters covering the full 60×60 -cm front of the Čerenkov-counter array. G_1 was used to identify events in which the detected photons were either accompanied by another charged particle, or in which the photons converted in the walls of the vacuum chamber or surrounding material.

Hodoscope G_2 was a double-layered matrix of scintillation counters covering the full face of the lead-glass array. Each layer was made up of 12 counters arranged either parallel or perpendicular to the plane of the beams. The coincidence between signals from the two layers of G_2 was used as a trigger for photons which converted in the lead sheet and provided time-of-flight information.

An additional hodoscope, G_3 , was mounted immediately behind the lead-glass Čerenkov counters, and was used to trigger on charged particles which completely traversed the photon detector. Such runs were used for calibration purposes throughout the course of the experiment. In addition to the scintillators mentioned above, two "guard" counters G_4 and G_5 were present when the photon detector was located at $\theta = 90^\circ$. Each was arranged so that it completely shadowed the side

of the Čerenkov array, as seen from the upstream direction along either incoming beam pipe. Each of these counters was sandwiched between two 5-cm-thick lead walls. It was found experimentally that single-beam background events often entered the photon detector from the sides. The lead walls were useful in reducing this source of background, and counters G_4 and G_5 were used to tag those events in which a particle traversed these walls. These counters and lead walls were unnecessary in the forward-angle positions since, for these data, the detector time-of-flight information was sufficient to eliminate this source of background.

The energy calibration of the Čerenkov counters was performed in a test beam at the CERN Proton Synchrotron. In this calibration,⁶ the pulse area of the signals produced in the Čerenkov counters by incident electrons of known momentum was compared to the pulse areas produced by a standard source of pulsed light. For the purposes of this calibration, it was assumed that the test-beam electrons produced electromagnetic showers which were similar to the showers produced by photons of the same energy. In this way one can calculate the electron equivalent energy of the light source, and, since the source is reproducible, use this same source to monitor the calibration of the Čerenkov counters after they were installed at the ISR.

The following three different sources of pulsed light were used: radioactive $^{241}\text{Am-NaI(Tl)}$ light-pulse sources, light-emitting diodes, and the Čerenkov light due to relativistic hadrons fully traversing the detector. The Čerenkov-counter calibrations as determined by these procedures are estimated to have an overall scale uncertainty of $\pm 5\%$ for the data taken at $\theta = 90^\circ$ and 17.5° , and $\pm 7\%$ at $\theta = 8^\circ$. The energy resolution as measured in the test beam was found to be parameterized well by $\Delta E/E = 0.14/\sqrt{E}$, where ΔE is the full width of half maximum, and E is the energy in GeV. It was established that the lead-glass system and its integrating electronics were linear to within 1%.

The trigger for this experiment contained three components:

$$\text{trigger} = (BB) \cdot (G_2) \cdot (LG).$$

BB denotes the beam-beam interaction trigger, in which at least one charged-particle coincidence was demanded in the hodoscopes H_1-H_4 or TB in both left and right hemispheres.⁷ BB is sensitive to about 95% of the inelastic cross section. G_2 is the twofold coincidence of the planes of G_2 preceding the lead-glass blocks. LG represents the requirement that a summed pulse area from the 16 lead-glass blocks be above some preset value. This value was changed frequently so as to collect

data for various regions of p_1 . Special runs were taken with trigger = (BB) or with trigger = $(BB) \cdot (G_2)$ in order to obtain the unbiased distributions. The time resolution of the trigger was about ± 30 nsec.

For each trigger, the times of all trigger elements present were recorded so that more restrictive time cuts could be made in analysis. Each hodoscope counter which detected a charged secondary in coincidence with the trigger caused a latch bit to be set. The signals present in the 16 lead-glass Čerenkov counters were integrated, and the pulse area for each was recorded. All of this information was written on magnetic tape for subsequent analysis.

III. DATA ANALYSIS

Data at all energies and angles were analyzed in the same way, except that for data at $\theta = 17.5^\circ$ and 8° , the guard counters G_4 and G_5 were not employed.

A. Event selection

Our aim in the analysis of the data was to select events, in an unbiased manner, in which a photon was present with well-determined energy. A complication arises because the photon is, in general, accompanied by a number of charged particles. If such charged particles enter the lead-glass array, the determination of photon energy is distorted. If events in which charged particles are emitted near the photon direction are excluded, the event sample is biased owing to the known short-range correlations. In our experiment, the presence of such charged particles was signaled by a count in the G_1 hodoscope in front of the lead converter. However, a signal from an element of G_1 did not ensure the presence of a charged particle, owing to the possibility of photon conversions in the ISR vacuum pipe, G_1 itself, or in intervening material. There were also counts in G_1 owing to photon showers in the lead converter which leaked back into G_1 . The experiment was performed without any trigger requirement on G_1 so that we could study its effect in the off-line analysis.

In order to explore the sensitivity of our results to these effects, the data were analyzed to two different methods. In the first method, events with a G_1 counter struck were rejected, and consequently only photon triggers were accepted. For these events, the energy measurement in the lead-glass array was precise, and the transverse momentum was unambiguously determined. The photons in these events are almost entirely due to the decay of a single π^0 (or η^0); moreover, they are substantially free from any sources of neutral back-

ground.⁸ For the data taken with the photon detector at $\theta = 90^\circ$, the G_1 veto requirement eliminated about two-thirds of the events passing all other requirements owing to the presence of charged particles in G_1 or photon conversions. This rejection was found to be essentially independent of the energy detected in the lead-glass Čerenkov counters and increased only slowly with the c.m. energy of the incident protons. However, the G_1 veto requirement did reduce by a small amount the charged multiplicities detected around $\theta = 90^\circ$ owing to the known correlations. Similarly, the data taken with the photon detector at more forward angles exhibit reduced multiplicities in the region of the veto counter G_1 . However, these effects were observed to be much smaller than those present at $\theta = 90^\circ$.

The second analysis of the data at 90° was performed with no requirements placed on G_1 or on any other counters around the photon detector. This analysis avoided possible biases associated with the rejection of events in which charged particles struck G_1 , but introduced uncertainties in the identification of particles entering the photon detector, and in the measurement of their transverse momentum. Charge particles, for example, typically deposited about 530 MeV in the lead-glass Čerenkov counters even though their actual energy could have been much higher. The annihilation of an antinucleon in the lead-glass array could have simulated an event of very large transverse momentum. The steepness of the photon inclusive spectra in this case tends to increase the contamination from this source at any given p_1 . However, estimates of this source of high- p_1 events indicate that it is of negligible importance.⁸ Since charged particles deposit, on the average, less than their full energy in the lead-glass array and the average energy deposit by antinucleon annihilations has been found to be negligibly small, this unbiased analysis gives a transverse-momentum determination which is usually less than the sum of the transverse momenta of all particles entering the photon detector. Thus, high- p_1 events could still be correctly identified in this analysis.

None of our final results were found to depend significantly on which of the two complementary analyses were used. We have chosen to present results from the first analysis rather than the second simply because the first analysis cleanly identifies the incident particles as photons, and we can with greater accuracy determine their transverse momentum.

B. Random and single-beam backgrounds

The electronic trigger accepts two major sources of background. One occurs when a random

coincidence of signals satisfies the trigger requirements; the other is due to beam-gas collisions.

The beam-gas background events were separated from the events due to beam-beam collisions by measuring the time between all the signals that made up the trigger. The time-of-flight differences (TOF) between any two trigger hodoscopes were required to be within well-defined limits, providing the hodoscopes registered the presence of charged particles. Events due to beam-beam and beam-gas collisions are clearly resolved in these TOF distributions, in which the time resolution is about ± 2 nsec. As a result, very few beam-gas events satisfy the timing criteria used to select beam-beam events. Moreover, the fraction that do can be accurately estimated from data taken with only one ISR beam circulating. An upper bound on the number of random triggers accepted as beam-beam events was estimated from the TOF spectra, and was always less than 1%.

Although analysis of the hodoscope TOF's was by far the most powerful technique for eliminating background, for those data taken with the photon detector at $\theta = 90^\circ$, another method was found to be useful as well. It was found experimentally that many of the background events which simulated large- p_\perp triggers originated far from the crossing point and entered the lead-glass array from the side. By analyzing runs in which only one ISR beam was circulating, it was found that 90% of these background triggers were detected in either G_4 or G_5 . In the analysis of the neutral lead-glass data at $\theta = 90^\circ$ we have, therefore, rejected all events with a signal either in G_4 or G_5 . This additional requirement reduced the level of background contamination at this c.m. angle to less than 2% at all ISR energies, for p_\perp values below 4.5 GeV/c. The data taken at more forward c.m. angles contained even less background owing to the increased TOF separation at these positions. In all cases, the effect of the residual background on the multiplicity results presented was found to be negligible.

C. Transverse-momentum determination

The transverse momentum of the detected photons was determined from the energy deposited in the lead-glass array. For the data at $\theta = 17.5^\circ$ and 8° , the center of gravity of the electromagnetic showers in the lead-glass array was determined. Using this information and knowledge of the total energy deposited, the laboratory transverse momentum of the photons was determined. For the data taken at $\theta = 90^\circ$, the laboratory photon energy was taken to be equal to the total deposited energy, and the small corrections due to the exact shower

center of gravity locations were ignored. After the laboratory p_\perp was determined, p_\perp in the c.m. system was calculated. In the presentation of all our results, the data are presented in slices of 0.5-GeV/c width in p_\perp .

D. Multiplicity distributions

The multiplicities in the fixed regions of solid angle subtended by the hodoscope counters were computed by counting the total number of times the bit corresponding to each counter was set and dividing this number by the total number of events in the sample. This event total corresponded either to the total number of inelastic events with no photon required or to the total number of events with a photon observed in the lowest slice of p_\perp . These multiplicities were then normalized in the manner described below, and displayed as a function of the polar or azimuthal angle. The polar-angle distributions are plotted in bins of the pseudorapidity variable, $\eta \equiv -\ln[\tan(\theta/2)]$. This variable closely approximates the rapidity, $y \equiv \frac{1}{2} \ln(E + p_\parallel)/(E - p_\parallel)$, of the particle if $p^2 \gg m^2$.

E. Normalization

The measurement of the associated charged multiplicities as well as the angular distributions as a function of p_\perp have been normalized in two ways. The first consisted of dividing the distributions detected in events containing large- p_\perp photons by the corresponding distributions detected for events in which no requirements are placed on the photon detector (i.e., normal beam-beam collisions). The second normalization consisted of dividing the large- p_\perp distributions by those detected when the photon transverse momentum is small ($0 < p_\perp < 0.5$ GeV/c). Each normalization has advantages and disadvantages as will be discussed below. The reason for this choice of presentation of the data is the fact that an accurate measurement of absolute multiplicities in our experiment requires corrections for the systematic errors introduced by a variety of sources⁹: photon conversions, δ -ray production, and secondary strong interactions in the vacuum pipe and hodoscope structure, incomplete coverage of the solid angle, and possible bias associated with the G_1 , G_4 , or G_5 veto requirements. The net effect of these systematic errors is such that measured multiplicity distributions are approximately proportional to the true ones. The normalized results are thus expected to be quite accurate if changes in associated total or partial multiplicities with p_\perp are not large compared to the normalizing multiplicities. This condition is satisfied sufficiently well that the residual errors are small compared to the

observed effects.

The majority of the data on angular distributions has been normalized to our average inelastic multiplicities. This presentation has the advantage of being easily converted to "true" multiplicities simply by multiplying each distribution by the "true" average inelastic multiplicities. These "true" multiplicities can be computed from data collected by other ISR experiments, whose apparatus was such that they were able to measure accurately the inclusive single-particle spectra. Indeed, as will be discussed later, we have done this in order to extract certain results in terms of absolute multiplicities. This normalization also has the advantage of being related in a simple way to the well-known two-body correlation function.⁹ This normalized correlation function, $R(\eta_1, \eta_2)$, is defined to be

$$\begin{aligned} R(\eta_1, \eta_2) &= \frac{\sigma_{\text{inel}} d^2\sigma/d\eta_1 d\eta_2}{(d\sigma/d\eta_1)(d\sigma/d\eta_2)} - 1 \\ &= \frac{N_{\text{inel}} N_2(\eta_1, \eta_2)}{N_1(\eta_1) N_1(\eta_2)} - 1 . \end{aligned}$$

Here N_{inel} is the measured counting rate of inelastic $p\bar{p}$ collisions, $N_1(\eta)$ is the rate for a single charged particle at η , and $N_2(\eta_1, \eta_2)$ is the rate for a charged particle at both η_1 and η_2 within the same event.

Now if $M(\eta_1; \eta_2, p_\perp)$ is the multiplicity at η_1 when photons are detected at η_2 with transverse momentum p_\perp , normalized to the multiplicity at η_1 in the average inelastic event, we have

$$M(\eta_1; \eta_2, p_\perp) = \frac{N_2(\eta_1; \eta_2, p_\perp)}{N_1(\eta_2, p_\perp)} \frac{N_{\text{inel}}}{N_1(\eta_1)} .$$

where all quantities are defined as above with the exception that the photon at η_2 is constrained to have fixed transverse momentum p_\perp . Thus, in analogy with the above definition, we define the two-body correlation function with one particle of known transverse momentum to be

$$R(\eta_1; \eta_2, p_\perp) = M(\eta_1; \eta_2, p_\perp) - 1$$

and note that, owing to the sharply falling nature of the spectrum as a function of p_\perp , $R(\eta_1; \eta_2, p_\perp) \simeq R(\eta_1, \eta_2)$ for small p_\perp (i.e., $\lesssim 0.5$ GeV/c). The results presented in the next section on normalized multiplicities will be labeled $R(\eta_1; \eta_2, p_\perp) + 1$ accordingly.

However, this normalization masks somewhat the changes in the multiplicities as a function of p_\perp . Hence, for a portion of the data, we shall normalize to the data with a photon at low p_\perp ($0 < p_\perp < 0.5$ GeV/c). This normalization has the advantage of dividing out the effects of the "normal" low- p_\perp two-body correlation function, so that one

can see more clearly effects as a function of p_\perp . In particular, if there were any p_\perp -dependent effect in the rate of particle production opposite the photon in the c.m., one might hope to see it more clearly with this normalization. However, the two-body correlation at small p_\perp depends on the angle at which the photon is required (i.e., it is symmetric in η at $\theta = 90^\circ$, and not at 17.5° and 8°). This normalization, consequently, tends to obscure the behavior of the "absolute" multiplicity distributions as a function of p_\perp . We hope that presenting both normalizations for a portion of the data taken at $\sqrt{s} = 53$ GeV will help the reader to gain a better understanding of the observed effects. We emphasize that the words "normalized multiplicity" will mean normalized to the average inelastic multiplicities, except for that small portion of the text where this second normalization is specifically discussed.

F. Corrections and residual errors

The data on associated charged multiplicities and angular distributions have been corrected for two systematic effects.

The first effect is due to the finite spatial resolution of the counters used to measure the associated multiplicity. In particular, there is some probability that more than one particle will strike the same counter in a single event. Under such circumstances several secondaries would be counted as only one, and would, as a result, cause the measured multiplicity to be lower than the true multiplicity. Since this effect depends quadratically, rather than linearly, on the detected average multiplicity, our normalization is not effective in totally removing this systematic error. Consequently, we have corrected the experimentally measured multiplicities *before normalization*. The multiplicities thus corrected contain less than a 5% error from this source *before normalization*. The *normalized* multiplicities which are presented are expected to contain $\lesssim 1\%$ systematic error from this source.

The second correction applied to the associated multiplicity data is that necessary to transform the data to the c.m. frame. Since our small-angle hodoscopes $H_4\theta$ and $H_2\theta$ surround the exiting beam pipe, these data are affected very little by this correction. The L hodoscope, on the other hand, is symmetric with respect to the beam bisector, and consequently the correction is much larger in this region. The correction for c.m. motion was taken from the data by requiring that the beam-beam events display an azimuthal symmetry.

Finally, for the data normalized to the average inelastic multiplicities, there is one additional

systematic effect. This occurs because of the bias arising from the requirement that no count be recorded in the hodoscope G_1 , which precedes the lead converter. The imposition of a G_1 veto has two effects. It slightly reduces the multiplicity of charged particles near the photon rapidity, owing to the short-range correlations. It also decreases the average inelastic multiplicities near $\theta = 90^\circ$ owing to a suppression of large-multiplicity (pionization) events relative to low-multiplicity (diffractive) events. The net effect is to *increase* the multiplicities normalized to average inelastic events by about 10% for $|\eta| \lesssim 1$ for the data with the photon near $\theta = 90^\circ$. Data for photons at the forward angles are considerably less affected; data normalized to multiplicities at low p_\perp are also unaffected. No correction has been applied to the data for this effect.

IV. RESULTS

In the first part of this section, we shall present the distributions of normalized partial multiplic-

ities as a function of both the polar and the azimuthal emission angles of the detected secondaries.

While data were taken and analyzed at all the ISR energies, $\sqrt{s} = 23, 31, 45, 53,$ and 62 GeV at $\theta = 90^\circ, 17.5^\circ,$ and 8° , we will summarize by presenting results on the distributions at $\sqrt{s} = 23$ and 53 GeV only. Discussion of the s dependences and associated multiplicities will include data for all energies. In order to see more clearly the effects of the transverse-momentum balancing process, we have examined the multiplicities and distributions separately in the azimuthal hemispheres away from and toward the observed photon.

Figures 3 and 4 display the normalized partial multiplicities as a function of η for various bins in the transverse momentum of photons detected near $\theta = 90^\circ$ ($|\eta| \leq 0.25$). As stated above, these multiplicities have been divided by the corresponding multiplicities with no photon required. With this normalization, effects due to two-particle correlations between photons and charged particles are made apparent. We see, in these figures,

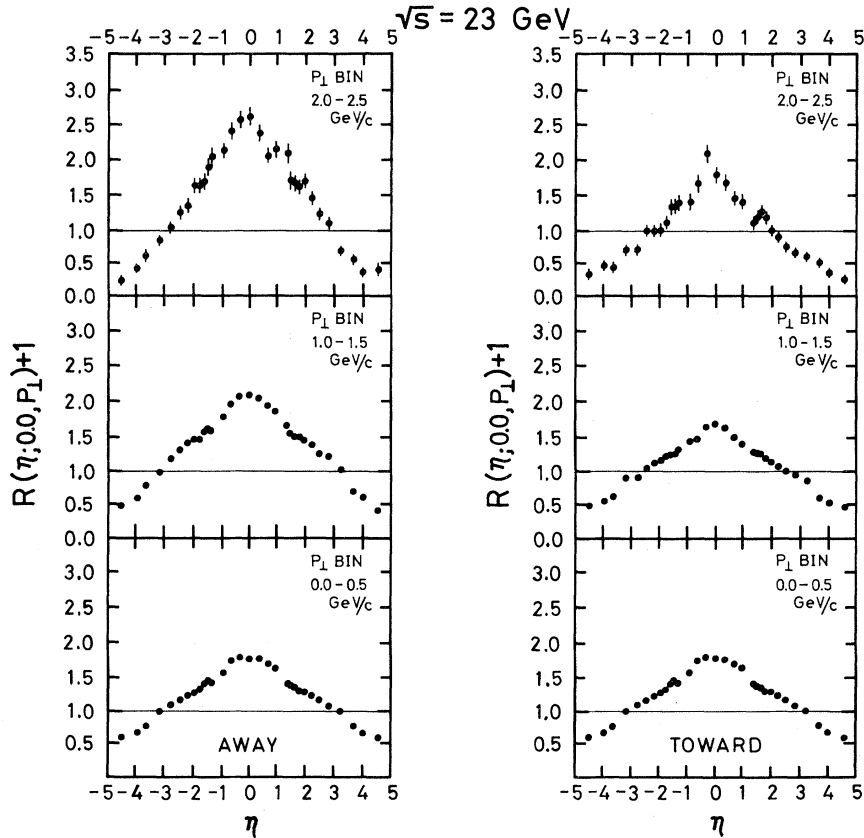


FIG. 3. Multiplicity distribution normalized to inelastic events at $\sqrt{s} = 23$ GeV versus η . The photon is detected at $\eta \approx 0$. The hemispheres away and toward the photon in azimuth are plotted separately. The p_\perp of the photon is indicated in the figure.

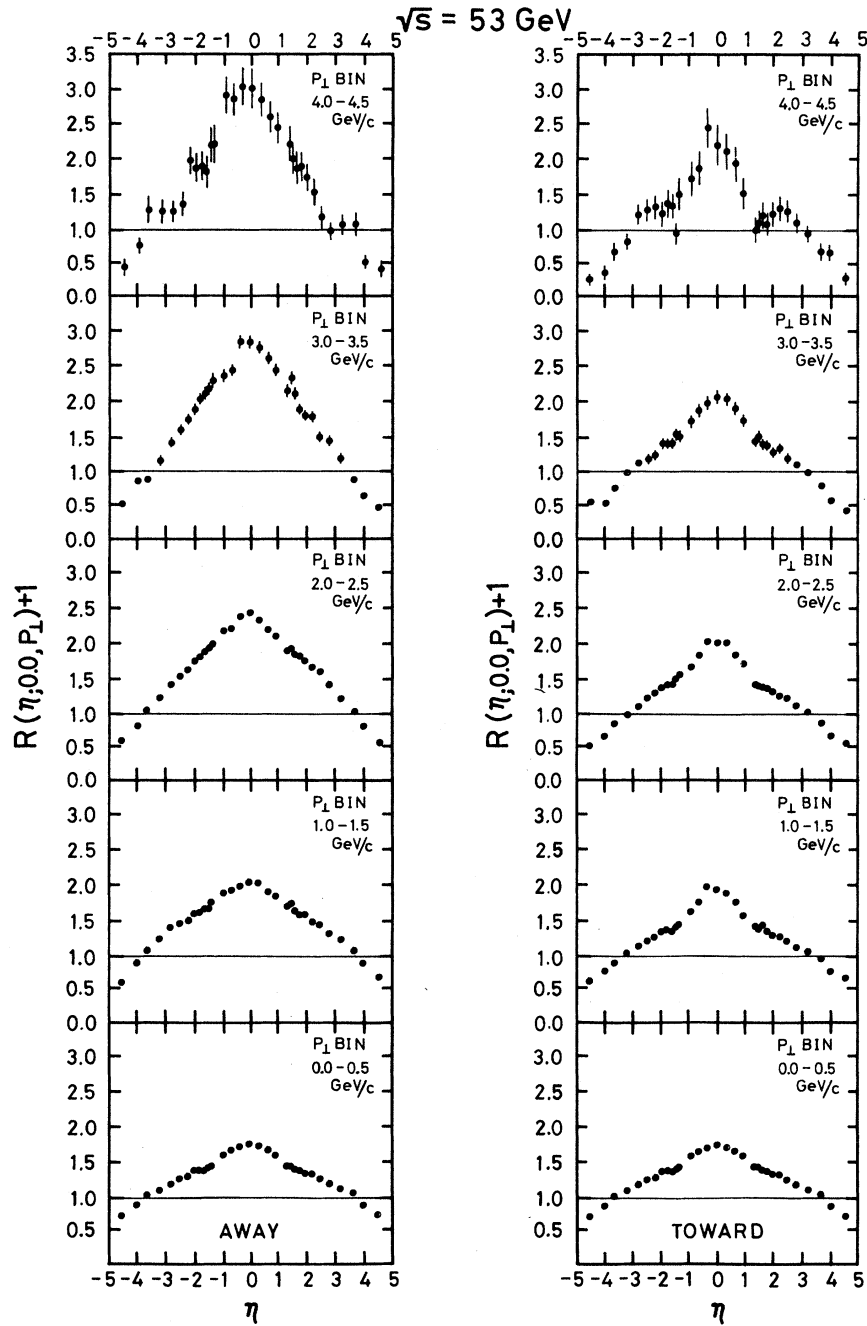


FIG. 4. Same as for Fig. 3, except that $\sqrt{s} = 53$ GeV.

that there is a clear effect due to these correlations which produces a local increase around the η of the photon when p_{\perp} is small. The normalized multiplicities away from the detected photons increase above this level with increasing p_{\perp} over a broad angular range for both energies. The multiplicities at small forward angles decrease with increasing p_{\perp} over the full azimuth. Finally, the

multiplicities near $\theta_{c.m.} = 90^\circ$ toward the detected photon show only a very small increase for $\sqrt{s} = 53$ GeV, while at 23 GeV they decrease by about 15% in this region.

The data of Figs. 3 and 4 tend to have a small dip for the toward-hemisphere partial multiplicities near $|\eta| = 1$. This effect could be due, in part, to particles generated in the photon shower in the

lead converter and lead-glass array which “splash” back into the nearby L counters. However, those transverse-momentum bins which are not shown in Figs. 3 and 4 show less of this structure. We do not attach significance to these dips. The value of $R(0,0)+1$ for $0 \leq p_{\perp} \leq 0.5$ GeV/c is about 1.75 in both toward and away hemispheres. This is about 10% larger than the value quoted for inclusive charge-charge or photon-charge correlations.⁹ We attribute this difference to the effect of the G_1 bias discussed in Sec. III.

Figures 5 and 6 display distributions similar to Figs. 3 and 4, except that, for these data, the large-transverse-momentum photons were detected at $\theta \approx 17.5^\circ$ ($\eta \approx 1.9$). As before, at small p_{\perp} , the two-body correlation causes a local increase in the multiplicities near $\eta = 1.9$. However, the effects of increasing p_{\perp} are different for these data. In particular, the multiplicities rise more for negative η (charged particles in the opposite polar hemisphere to the photon). This increase again extends over an appreciable η region. In addition, we note that this increase is even seen

to some extent in the “toward” azimuthal hemisphere, and, furthermore, that the distributions at large p_{\perp} are close to symmetric about $\eta = 0$ even though the photon was detected at $\eta = 1.9$. Finally, as in the 90° data, the multiplicities at small forward angles are seen to decrease rapidly with increasing p_{\perp} .

Figures 7 and 8 show the same η distributions for data in which the large- p_{\perp} photons were detected at $\theta \approx 8^\circ$ ($\eta \approx 2.7$). As can be seen from the figures, these distributions look similar to those obtained with the photon detector at 17.5° . However, there are several differences. The associated multiplicity near the detected photon is seen to decrease very rapidly with the increasing p_{\perp} of the photon. The effect is particularly prominent at the lower energy, $\sqrt{s} = 23$ GeV, and thus is likely due to kinematic effects; the rapid increase in longitudinal momentum p_{\parallel} that corresponds to increasing p_{\perp} at these angles removes the energy from the rest of the event. It seems that this is done predominantly at the expense of the other secondaries in the same polar hemisphere as the

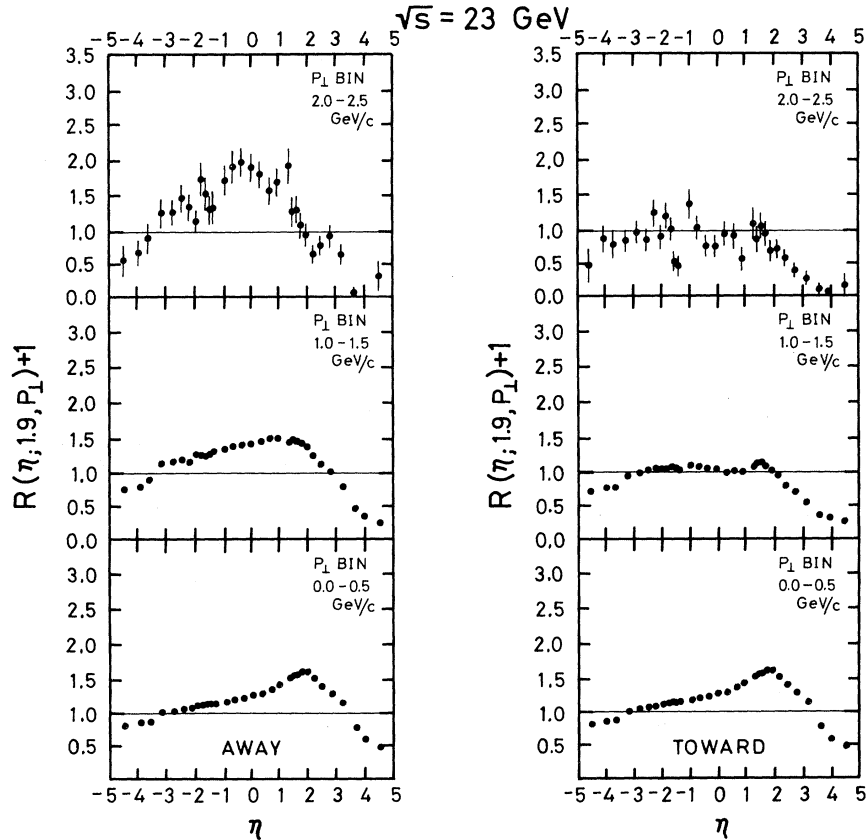


FIG. 5. Multiplicity distribution normalized to inelastic events at $\sqrt{s} = 23$ GeV versus η . The photon is detected at $\eta \approx 1.9$. The hemispheres away and toward the photon in azimuth are plotted separately. The p_{\perp} of the photon is indicated in the figure.

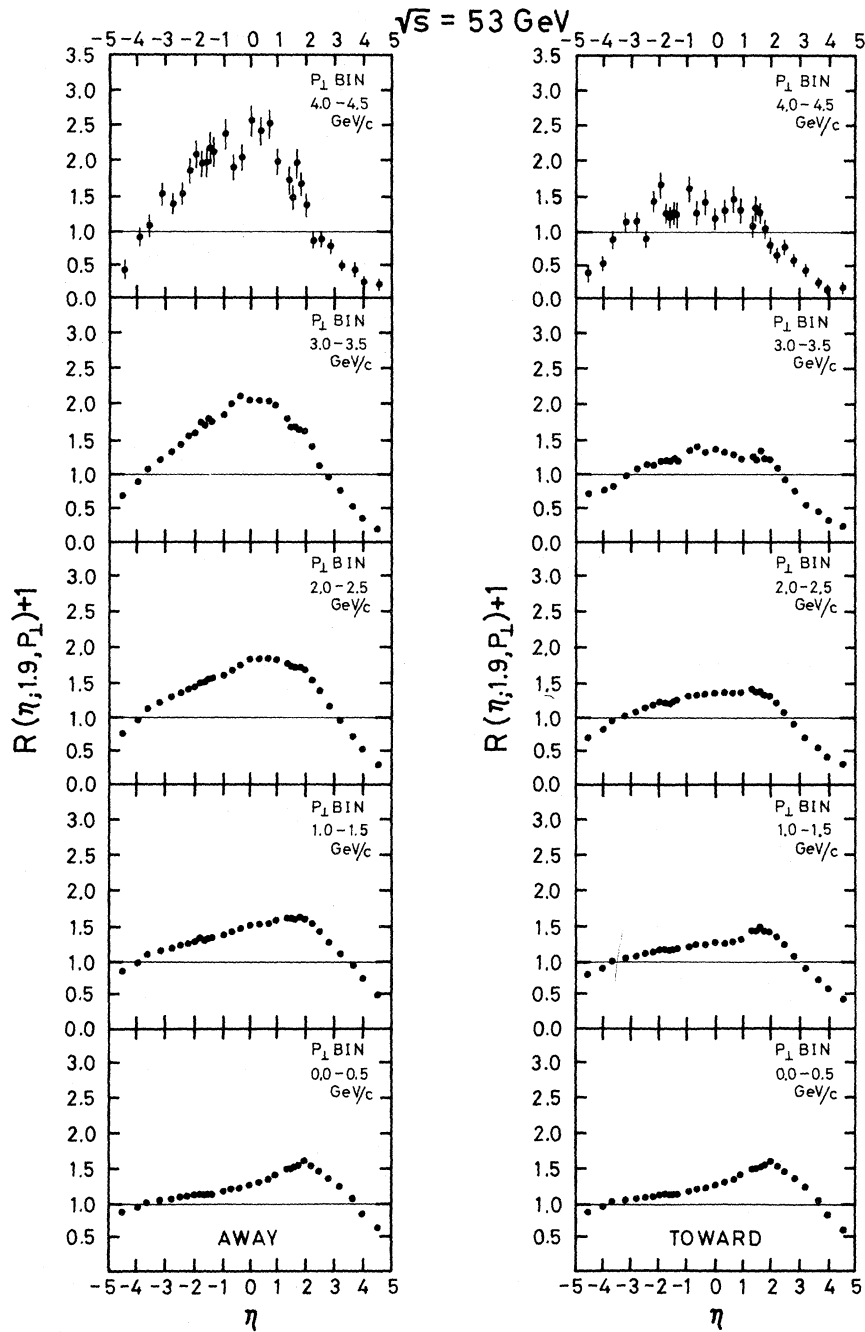


FIG. 6. Same as for Fig. 5, except that $\sqrt{s} = 53$ GeV.

detected photon. We note also that, as p_{\perp} increases, the familiar short-range correlation observed in inclusive events becomes less apparent, especially in the azimuthal hemisphere away from the detected photon.

Next we present the same angular distributions normalized in the second way. This normalization, as discussed in the preceding section, con-

sists of dividing all the particle multiplicities by their corresponding values at low p_{\perp} ($0 \leq p_{\perp} \leq 0.5$ GeV/c). This normalization removes the γ -charged correlations present at low p_{\perp} , and allows a clearer picture of the p_{\perp} dependence itself. In particular, if there were any strong "back-to-back" balancing of transverse momenta, then one would expect to see it most clearly with this nor-

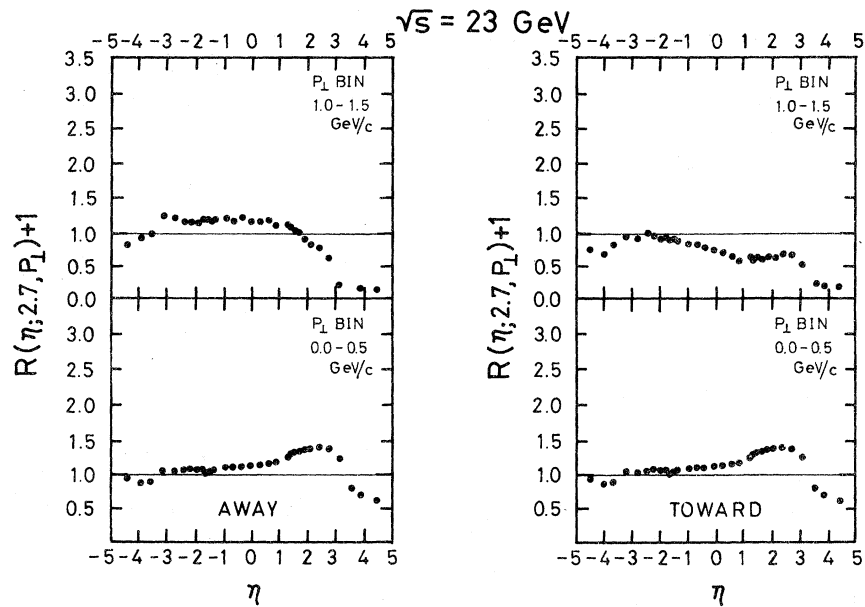


FIG. 7. Multiplicity distribution normalized to inelastic events at $\sqrt{s} = 23$ GeV versus η . The photon is detected at $\eta \approx 2.7$. The hemispheres away and toward the photon in azimuth are plotted separately. The p_1 of the photon is indicated in the figure.

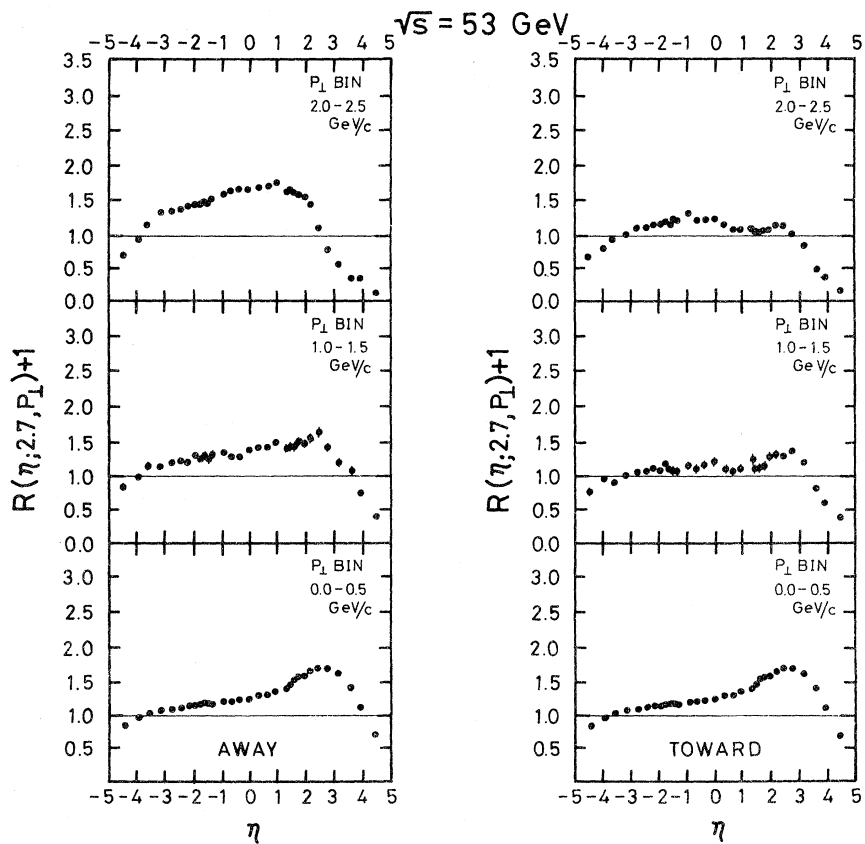


FIG. 8. Same as for Fig. 7, except that $\sqrt{s} = 53$ GeV.

malization. For the sake of brevity, only the data at $\sqrt{s} = 53$ GeV are presented. The data at other c.m. energies are quite similar. In Fig. 9, the associated multiplicities normalized in this way

are shown for all three photon-detector positions. For 90° photons, we see that the *growth* in the associated multiplicities is centered about $\theta = 90^\circ$ ($\eta = 0.0$) in the hemisphere opposite the photon,

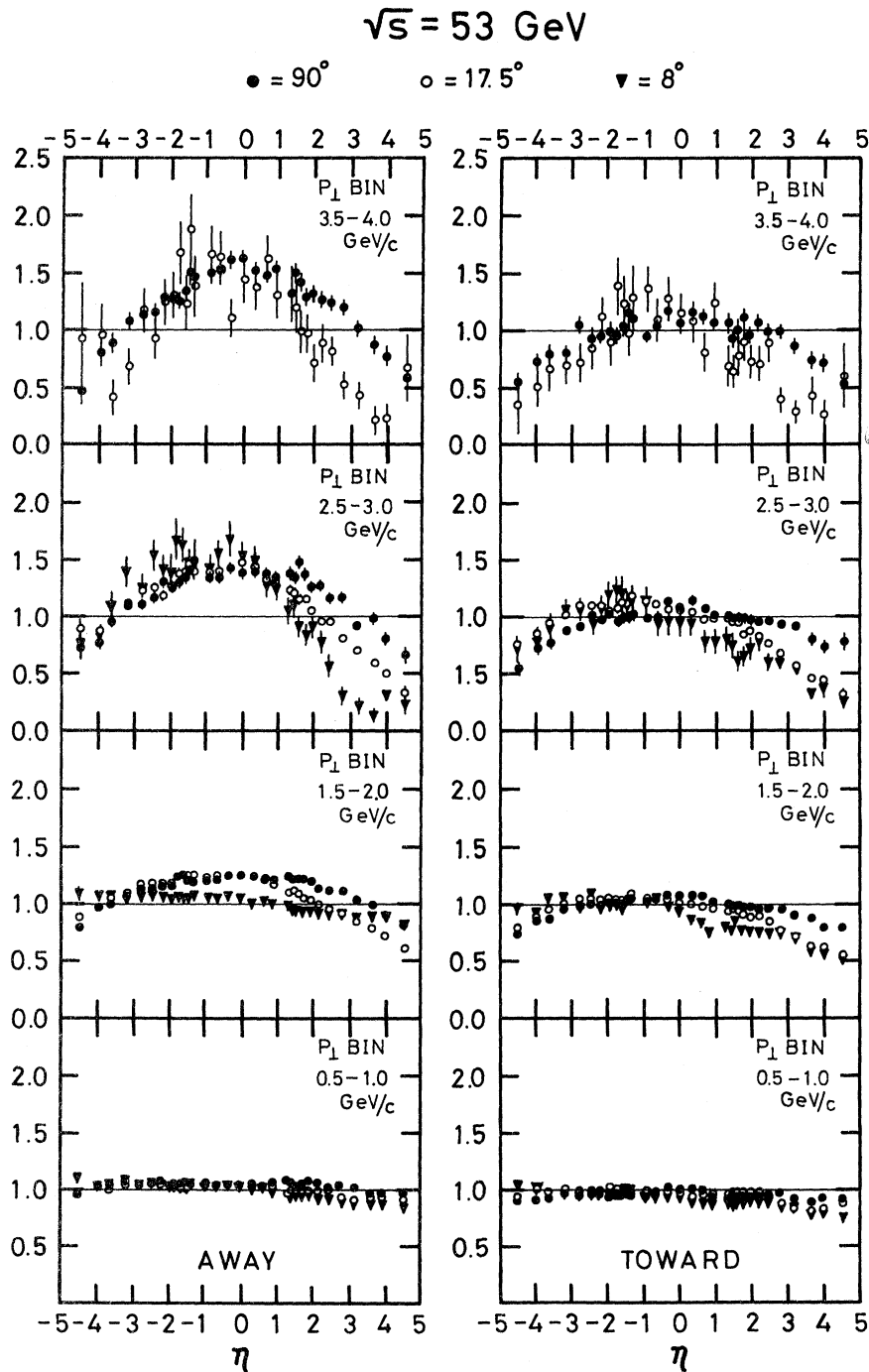


FIG. 9. Multiplicity distributions, normalized to the values observed in events with p_{\perp} of the photon ≤ 0.5 GeV/c, versus η , for $\sqrt{s} = 53$ GeV. The hemispheres away from and toward the photon in azimuth are plotted separately. The p_{\perp} of the photon is indicated in the figure. ●: photon rapidity ≈ 0 ; ○: photon rapidity ≈ 1.9 ; ▼: photon rapidity ≈ 2.7 .

and is quite broad. Roughly half of this growth is contained in the θ interval from 40° to 140° . The lack of any appreciable growth in the multiplicities near $\theta = 90^\circ$ in the hemisphere toward the detected photon is evident in this figure. For the 17.5° ($\eta = 1.9$) photons, the multiplicity increases again primarily in the hemisphere away from the detected photons. However, there is some observable increase even in the "toward" hemisphere. The increase in the multiplicity in the "away" hemisphere is largest at $\eta = -0.7$, and has a width similar to that of the 90° data. Finally, the data taken with the photon detector at 8° ($\eta = 2.7$) look quite similar to that at 17.5° , except that now the increase is centered at $\eta = -1.0$. Thus, we observe a tendency for the associated multiplicities to increase in a broad region, which is more or less opposite, but not "back-to-back" in the c.m. system. This behavior may be a reflection of the dynamical mechanism for producing these particles. On the other hand, there are also strong kinematical effects present in the 17.5° and 8° data: Observation of a large- p_\perp photon implies a longitudinal component $p_\parallel \approx 3p_\perp$ when the photon is detected at $\theta = 17.5^\circ$, while for the 8° data, $p_\parallel \approx 7p_\perp$. Thus, the rest frame of all particles except the photon moves toward negative η .

Next we turn to an examination of the azimuthal distribution of the secondaries. We consider first the data taken with the photon detector at $\theta = 90^\circ$. In Fig. 10, we show the partial multiplicities normalized to average inelastic events in the interval $-0.7 < \eta < 0.7$ (i.e., around $\theta = 90^\circ$) for the 20 ϕ bins of L hodoscope. The azimuthal position of each bin is given with respect to the center of the lead-glass array, and has been transformed to the c.m. frame assuming that $\beta = 1$ for all particles. This correction for the c.m. motion is approximate since not all particles near $\theta = 90^\circ$ are relativistic. However, the results reported here are insensitive to this correction. From this figure, we see quite clearly that the multiplicity increases with p_\perp in a fairly broad azimuthal region opposite the detected photon. The full width of this distribution is about 120° at half height, and seems to be independent of p_\perp and \sqrt{s} . This width is much broader than the ϕ width subtended by the photon detector ($\pm 14^\circ$). Next we consider the data taken with the photon detector at $\theta = 17.5^\circ$ and 8° . The ϕ distributions for these data are presented in Fig. 11. These data are divided into three polar angle regions: $1.3 \leq \eta \leq 1.9$, $-0.7 \leq \eta \leq 0.7$, and $-1.9 \leq \eta \leq -1.3$. For the data at 17.5° , the photon is detected at $\eta \approx 1.9$; thus, we examine in detail the ϕ distributions both at η 's near the photon and opposite it in the c.m. We note that the azimuthal asymmetry increases as p_\perp increases for *all* regions of η .

Therefore, it seems that p_\perp is being balanced over the entire hemisphere azimuthally away from the photon. The width of the azimuthal region containing the increase is roughly independent of the polar-angle region, the c.m. energy, and the polar angle of the detected photon and of similar magnitude as in the 90° data.

We estimate an overall systematic error for all the preceding results on normalized multiplicities to be $\pm 10\%$.

Next we turn to the question of computing *absolute* multiplicity distributions from these data. Since the normalized multiplicities which we have presented are expected to be quite accurate, what is required is accurate data on the *normalizing*

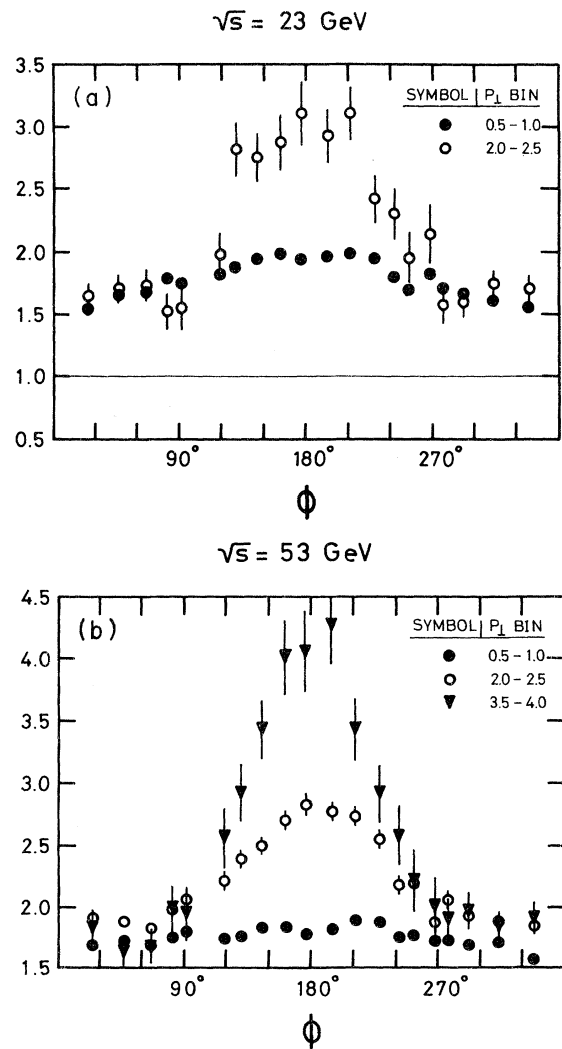


FIG. 10. Multiplicity distributions normalized to inelastic events versus ϕ , in the interval $|\eta| \leq 0.7$. The photon is detected at $\eta \approx 0$ and $\phi \approx 0^\circ$. (a) $\sqrt{s} = 23$ GeV, (b) $\sqrt{s} = 53$ GeV.

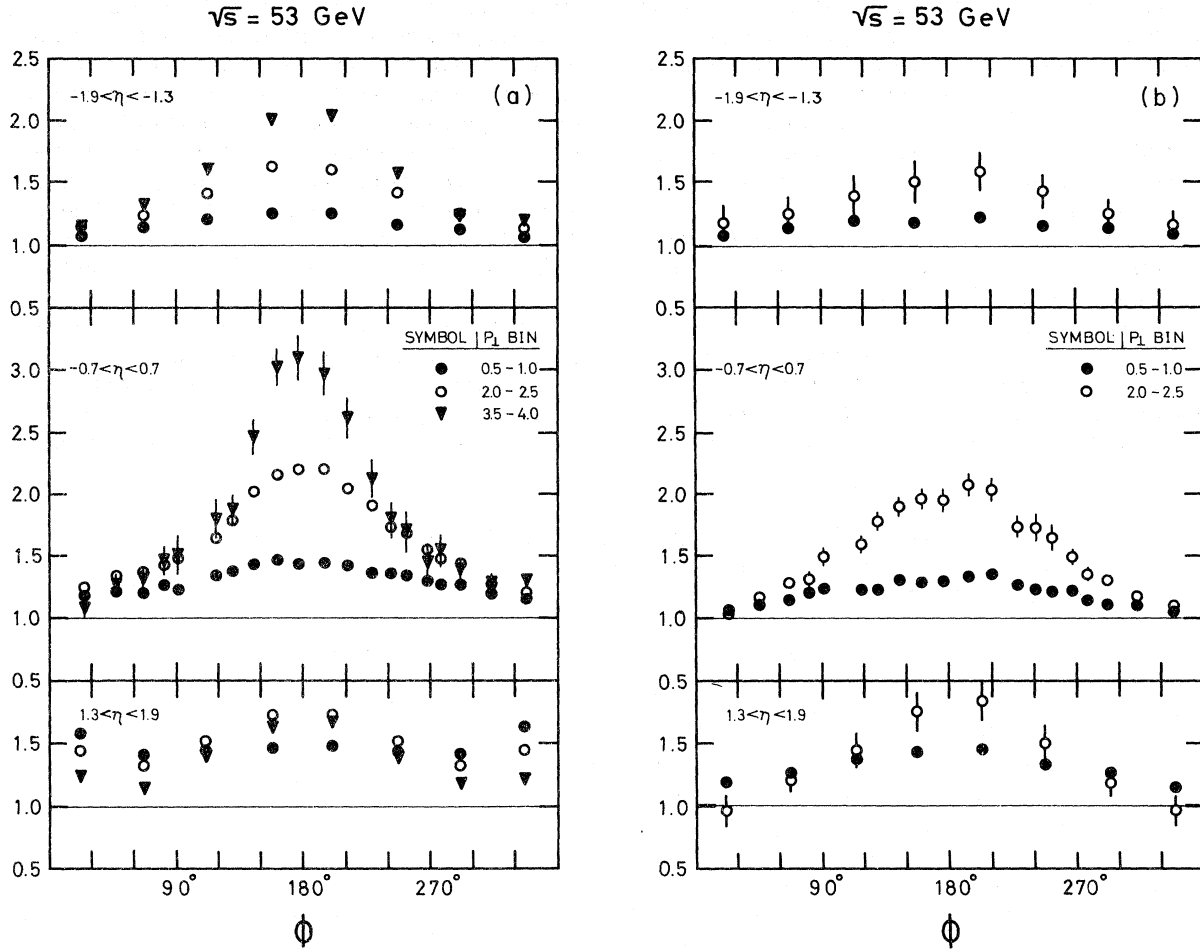


FIG. 11. Multiplicity distributions normalized to inelastic events versus ϕ at $\sqrt{s}=53$ GeV. The photon direction is $\phi \approx 0^\circ$. Three regions of η are shown for various p_\perp . (a) photon rapidity ≈ 1.9 , (b) photon rapidity ≈ 2.7 .

multiplicities. A number of groups¹⁰ working at the ISR have measured the single-particle cross sections, $E d^3\sigma/dp^3$, for various particle types so that data exist for nearly the full solid angle. These experiments are such that their statistical and systematic errors were small, allowing them to produce accurate cross sections for these dominantly low- p_\perp processes.¹¹ Combining these data with information on the p_\perp dependence (at small p_\perp) of the various particle types, we have extracted single-particle differential cross sections $d\sigma(\eta)/d\eta$, summarizing all the available data. The cross sections thus obtained are listed in Table II for all five ISR energies. These spectra were divided by the average inelastic cross sections at each energy, and then used to multiply the normalized multiplicities $M(\eta_1; \eta_2, p_\perp)$.

The differential multiplicity distributions computed in this way are expected to be free of most of the systematic errors associated with our experiment, and are estimated to have an overall

TABLE II. "Best" charged particle ($d\sigma/d\eta$) (mb) for average inelastic events.

η	\sqrt{s} (GeV)	23	31	45	53	62
0.00		42.88	43.57	44.60	45.06	45.53
0.34		42.74	43.46	44.48	44.93	45.40
0.65		43.41	44.23	45.31	45.76	46.23
0.92		44.10	45.18	46.40	46.86	47.33
1.34		44.53	46.11	47.90	48.44	49.00
1.46		44.27	46.20	48.19	48.79	49.35
1.60		43.63	46.08	48.29	49.09	49.68
1.76		42.51	45.55	48.25	49.13	49.95
1.95		40.43	44.27	47.98	48.95	49.85
2.19		36.93	41.68	46.78	48.24	49.42
2.46		32.29	37.57	44.19	46.30	48.11
2.79		27.48	31.73	39.21	42.20	44.82
3.19		20.75	25.43	31.90	35.06	38.34
3.65		12.87	17.73	24.26	27.36	30.09
4.20		6.49	9.18	14.78	17.84	20.74
4.74		3.02	4.43	7.60	9.33	11.43

systematic uncertainty of $\pm 20\%$, including the error associated with the normalizing multiplicity distributions. These differential multiplicities are listed in Tables III–VIII for the three photon-detector positions. They are tabulated as functions of p_{\perp} and η , and are given separately for the azimuthal hemispheres away from and toward the detected photon.

From these differential multiplicity distributions, we can then go on to compute the associated total multiplicities, $M(\eta_2, p_{\perp})$, by integrating $dN(\eta_1; \eta_2, p_{\perp})/d\eta_1$ over η_1 .

The associated total multiplicities calculated in this way are presented in Fig. 12 for the data taken with the photon detector at $\theta = 90^\circ$. We see that the total multiplicity increases with increas-

ing p_{\perp} , and that this increase is largest at $\sqrt{s} = 62$ GeV, where the multiplicity grows approximately linearly with p_{\perp} . The data at the three highest energies exhibit a similar p_{\perp} dependence for $p_{\perp} < 3.0$ GeV/c. At $\sqrt{s} = 45$ and 53 GeV, where the data extend to larger p_{\perp} , we observe that the rate of growth of the total multiplicity decreases as p_{\perp} increases. The multiplicity at $\sqrt{s} = 23$ and 31 GeV show first a decrease at low p_{\perp} which changes to a relatively small increase at higher p_{\perp} .

In order to understand this behavior, we have computed separately the multiplicities in the hemisphere away from and toward the photon detector. These hemisphere multiplicities are plotted vs p_{\perp} in Figs. 13 and 14 for the 90° photon

TABLE III. Differential multiplicity distributions for away and toward hemispheres. Photon detector is at 90° , and $\sqrt{s} = 23$ GeV.

Away hemisphere $dN/d\eta$						
η	p_{\perp} (GeV/c) 0.0-0.5	p_{\perp} (GeV/c) 0.5-1.0	p_{\perp} (GeV/c) 1.0-1.5	p_{\perp} (GeV/c) 1.5-2.0	p_{\perp} (GeV/c) 2.0-2.5	p_{\perp} (GeV/c) 2.5-3.0
-4.74	0.029 ±0.002	0.027 ±0.001	0.022 ±0.001	0.018 ±0.002	0.012 ±0.003	0.019 ±0.013
-4.20	0.069 ±0.003	0.065 ±0.002	0.058 ±0.001	0.051 ±0.003	0.042 ±0.006	0.043 ±0.013
-3.65	0.153 ±0.006	0.153 ±0.004	0.137 ±0.004	0.136 ±0.007	0.126 ±0.015	0.103 ±0.029
-3.19	0.319 ±0.009	0.324 ±0.007	0.309 ±0.006	0.301 ±0.011	0.267 ±0.025	0.243 ±0.029
-2.79	0.464 ±0.012	0.479 ±0.009	0.494 ±0.009	0.473 ±0.015	0.442 ±0.033	0.453 ±0.073
-2.46	0.579 ±0.015	0.599 ±0.011	0.645 ±0.011	0.640 ±0.020	0.622 ±0.044	0.551 ±0.092
-2.19	0.697 ±0.017	0.756 ±0.013	0.785 ±0.013	0.810 ±0.023	0.760 ±0.052	0.701 ±0.111
-1.95	0.790 ±0.019	0.814 ±0.014	0.890 ±0.014	0.872 ±0.025	1.006 ±0.063	0.804 ±0.119
-1.76	0.863 ±0.021	0.901 ±0.016	0.933 ±0.016	0.997 ±0.029	1.046 ±0.069	0.959 ±0.147
-1.60	0.939 ±0.023	0.947 ±0.017	1.031 ±0.017	1.027 ±0.031	1.125 ±0.076	1.291 ±0.181
-1.46	0.989 ±0.024	1.011 ±0.018	1.085 ±0.018	1.125 ±0.032	1.298 ±0.080	1.409 ±0.175
-1.34	0.970 ±0.025	1.035 ±0.019	1.075 ±0.019	1.145 ±0.035	1.404 ±0.090	1.289 ±0.186
-0.92	1.058 ±0.019	1.103 ±0.014	1.190 ±0.014	1.361 ±0.031	1.436 ±0.073	1.582 ±0.179
-0.65	1.157 ±0.019	1.225 ±0.014	1.312 ±0.014	1.462 ±0.030	1.629 ±0.078	1.796 ±0.175
-0.34	1.175 ±0.020	1.233 ±0.015	1.358 ±0.015	1.469 ±0.037	1.704 ±0.081	2.099 ±0.205
0.00	1.161 ±0.021	1.269 ±0.016	1.380 ±0.017	1.494 ±0.033	1.745 ±0.083	2.279 ±0.222
0.34	1.157 ±0.020	1.235 ±0.015	1.335 ±0.016	1.463 ±0.032	1.566 ±0.075	1.664 ±0.178
0.65	1.128 ±0.019	1.203 ±0.014	1.288 ±0.015	1.432 ±0.030	1.391 ±0.067	1.571 ±0.168
0.92	1.103 ±0.019	1.173 ±0.014	1.262 ±0.014	1.391 ±0.030	1.478 ±0.073	1.464 ±0.166
1.34	0.965 ±0.026	1.060 ±0.020	1.126 ±0.020	1.206 ±0.037	1.442 ±0.095	0.995 ±0.162
1.46	0.932 ±0.024	1.010 ±0.018	1.042 ±0.018	1.134 ±0.034	1.164 ±0.082	1.138 ±0.165
1.60	0.909 ±0.023	0.929 ±0.017	0.987 ±0.017	1.091 ±0.033	1.108 ±0.072	0.950 ±0.152
1.76	0.850 ±0.021	0.919 ±0.016	0.964 ±0.016	1.022 ±0.029	1.054 ±0.068	1.011 ±0.157
1.95	0.804 ±0.019	0.851 ±0.014	0.898 ±0.014	0.923 ±0.026	1.062 ±0.064	0.775 ±0.114
2.19	0.706 ±0.017	0.732 ±0.013	0.779 ±0.013	0.825 ±0.024	0.826 ±0.053	0.974 ±0.135
2.46	0.585 ±0.015	0.592 ±0.011	0.620 ±0.010	0.696 ±0.020	0.620 ±0.044	0.486 ±0.089
2.79	0.461 ±0.012	0.488 ±0.009	0.510 ±0.009	0.473 ±0.015	0.472 ±0.034	0.470 ±0.077
3.19	0.323 ±0.009	0.328 ±0.007	0.326 ±0.006	0.314 ±0.012	0.226 ±0.022	0.285 ±0.056
3.65	0.158 ±0.006	0.162 ±0.004	0.141 ±0.004	0.137 ±0.007	0.118 ±0.014	0.071 ±0.024
4.20	0.069 ±0.003	0.067 ±0.002	0.060 ±0.002	0.054 ±0.003	0.039 ±0.006	0.031 ±0.012
4.74	0.029 ±0.002	0.027 ±0.001	0.020 ±0.001	0.019 ±0.002	0.021 ±0.005	0.001 ±0.000
Toward hemisphere $dN/d\eta$						
-4.74	0.029 ±0.002	0.024 ±0.001	0.022 ±0.001	0.017 ±0.002	0.016 ±0.004	0.013 ±0.007
-4.20	0.069 ±0.003	0.064 ±0.002	0.055 ±0.002	0.049 ±0.003	0.050 ±0.007	0.024 ±0.010
-3.65	0.153 ±0.005	0.135 ±0.004	0.118 ±0.003	0.094 ±0.005	0.086 ±0.013	0.073 ±0.024
-3.19	0.319 ±0.008	0.302 ±0.006	0.283 ±0.005	0.247 ±0.009	0.232 ±0.020	0.215 ±0.040
-2.79	0.464 ±0.012	0.417 ±0.008	0.376 ±0.007	0.351 ±0.012	0.302 ±0.025	0.285 ±0.057
-2.46	0.579 ±0.014	0.543 ±0.010	0.511 ±0.009	0.498 ±0.013	0.498 ±0.038	0.492 ±0.081
-2.19	0.697 ±0.018	0.637 ±0.012	0.631 ±0.011	0.607 ±0.020	0.570 ±0.044	0.605 ±0.097
-1.95	0.790 ±0.020	0.716 ±0.014	0.721 ±0.013	0.706 ±0.023	0.637 ±0.050	0.519 ±0.097
-1.76	0.863 ±0.021	0.823 ±0.015	0.803 ±0.014	0.814 ±0.024	0.757 ±0.052	0.943 ±0.126
-1.60	0.939 ±0.023	0.865 ±0.016	0.835 ±0.015	0.876 ±0.027	0.917 ±0.064	0.931 ±0.137
-1.46	0.989 ±0.026	0.858 ±0.018	0.843 ±0.017	0.830 ±0.030	0.918 ±0.070	1.013 ±0.165
-1.34	0.970 ±0.027	0.872 ±0.019	0.887 ±0.018	0.897 ±0.033	0.967 ±0.073	0.744 ±0.151
-0.92	1.058 ±0.031	1.011 ±0.023	0.971 ±0.022	0.976 ±0.035	0.974 ±0.076	1.037 ±0.182
-0.65	1.157 ±0.034	1.044 ±0.026	0.963 ±0.024	0.964 ±0.037	1.095 ±0.083	0.990 ±0.178
-0.34	1.175 ±0.033	1.117 ±0.025	1.058 ±0.024	1.044 ±0.037	1.366 ±0.091	0.876 ±0.155
0.00	1.161 ±0.031	1.156 ±0.024	1.089 ±0.023	1.056 ±0.036	1.329 ±0.086	1.329 ±0.189
0.34	1.157 ±0.031	1.096 ±0.024	1.057 ±0.023	1.037 ±0.036	1.106 ±0.080	0.757 ±0.148
0.65	1.128 ±0.032	1.042 ±0.024	0.976 ±0.023	1.010 ±0.037	0.967 ±0.076	0.899 ±0.166
0.92	1.103 ±0.032	0.944 ±0.023	0.928 ±0.023	0.866 ±0.035	0.939 ±0.078	0.802 ±0.149
1.34	0.965 ±0.028	0.925 ±0.020	0.867 ±0.018	0.858 ±0.032	0.762 ±0.067	0.746 ±0.139
1.46	0.932 ±0.025	0.891 ±0.018	0.857 ±0.017	0.856 ±0.029	0.826 ±0.069	0.630 ±0.124
1.60	0.909 ±0.023	0.864 ±0.016	0.843 ±0.015	0.815 ±0.026	0.883 ±0.058	0.831 ±0.135
1.76	0.849 ±0.022	0.794 ±0.015	0.772 ±0.014	0.786 ±0.026	0.785 ±0.059	0.590 ±0.108
1.95	0.804 ±0.021	0.717 ±0.014	0.692 ±0.013	0.698 ±0.024	0.624 ±0.050	0.526 ±0.103
2.19	0.706 ±0.017	0.625 ±0.012	0.603 ±0.011	0.596 ±0.020	0.514 ±0.041	0.724 ±0.111
2.46	0.585 ±0.014	0.515 ±0.009	0.485 ±0.009	0.466 ±0.016	0.378 ±0.031	0.417 ±0.079
2.79	0.461 ±0.012	0.417 ±0.008	0.392 ±0.007	0.365 ±0.013	0.287 ±0.026	0.412 ±0.068
3.19	0.323 ±0.008	0.299 ±0.006	0.268 ±0.005	0.243 ±0.009	0.199 ±0.018	0.196 ±0.040
3.65	0.158 ±0.005	0.133 ±0.003	0.114 ±0.003	0.106 ±0.006	0.104 ±0.013	0.092 ±0.026
4.20	0.069 ±0.003	0.062 ±0.002	0.052 ±0.001	0.044 ±0.003	0.038 ±0.006	0.044 ±0.013
4.74	0.029 ±0.002	0.024 ±0.001	0.021 ±0.001	0.017 ±0.002	0.013 ±0.003	0.009 ±0.006

data.

The multiplicities away from the high- p_{\perp} photon increase roughly linearly with p_{\perp} at all five energies. However, the hemisphere multiplicities toward the photon behave quite differently at different energies. In particular, at lower energies, there is a decrease in the “toward” multiplicities with increasing p_{\perp} . Even at the highest energy one sees only about a 4% increase.

V. PHENOMENOLOGICAL DISCUSSION

In this section, we discuss some of the results presented in the preceding section. In particular, we discuss only the data taken with the photon detected near $\theta = 90^\circ$, and examine the p_{\perp} and s dependences of the associated multiplicity.

As noted above, the number of charged particles produced in association with a high- p_{\perp} photon shows an increase over the number produced in events with a low- p_{\perp} photon. This increase is contained within a broad region of solid angle oriented opposite to the photon. The width of the increase in both η and ϕ is approximately independent of the p_{\perp} of the photon. The rate of increase in the away-hemisphere multiplicities with p_{\perp} is approximately the same at all \sqrt{s} (Fig. 13).

We find these facts suggestive of the following qualitative subdivision of the particles produced in collisions leading to high- p_{\perp} secondaries. We can envision three categories of particles:

A. a group of secondary collision products characteristic of ordinary (low- p_{\perp}) inelastic

TABLE IV. Differential multiplicity distributions for away and toward hemispheres. Photon detector is at 90° , and $\sqrt{s} = 53$ GeV.

Away hemisphere $dN/d\eta$									
η	p_{\perp} (GeV/c) 0.0-0.5	p_{\perp} (GeV/c) 0.5-1.0	p_{\perp} (GeV/c) 1.0-1.5	p_{\perp} (GeV/c) 1.5-2.0	p_{\perp} (GeV/c) 2.0-2.5	p_{\perp} (GeV/c) 2.5-3.0	p_{\perp} (GeV/c) 3.0-3.5	p_{\perp} (GeV/c) 3.5-4.0	p_{\perp} (GeV/c) 4.0-4.5
-4.74	0.095 ± 0.002	0.091 ± 0.003	0.074 ± 0.003	0.075 ± 0.002	0.075 ± 0.003	0.068 ± 0.007	0.065 ± 0.006	0.043 ± 0.009	0.057 ± 0.016
-4.20	0.222 ± 0.003	0.224 ± 0.004	0.209 ± 0.005	0.200 ± 0.004	0.183 ± 0.006	0.153 ± 0.010	0.190 ± 0.011	0.155 ± 0.018	0.159 ± 0.027
-3.65	0.394 ± 0.006	0.403 ± 0.008	0.399 ± 0.010	0.387 ± 0.008	0.379 ± 0.011	0.370 ± 0.022	0.323 ± 0.019	0.334 ± 0.034	0.471 ± 0.071
-3.19	0.540 ± 0.006	0.581 ± 0.010	0.592 ± 0.011	0.583 ± 0.009	0.589 ± 0.014	0.597 ± 0.027	0.549 ± 0.024	0.582 ± 0.042	0.595 ± 0.079
-2.79	0.699 ± 0.008	0.735 ± 0.012	0.805 ± 0.014	0.804 ± 0.012	0.814 ± 0.017	0.791 ± 0.033	0.807 ± 0.031	0.803 ± 0.056	0.724 ± 0.088
-2.46	0.815 ± 0.010	0.856 ± 0.014	0.926 ± 0.017	0.950 ± 0.014	0.981 ± 0.021	0.984 ± 0.042	1.016 ± 0.039	0.971 ± 0.065	0.871 ± 0.104
-2.19	0.869 ± 0.010	0.942 ± 0.015	0.987 ± 0.017	1.030 ± 0.015	1.075 ± 0.022	1.183 ± 0.046	1.146 ± 0.042	1.156 ± 0.073	1.306 ± 0.131
-1.95	0.938 ± 0.010	0.993 ± 0.016	1.071 ± 0.019	1.115 ± 0.016	1.175 ± 0.024	1.240 ± 0.049	1.267 ± 0.047	1.233 ± 0.079	1.255 ± 0.137
-1.76	0.948 ± 0.011	1.010 ± 0.017	1.094 ± 0.020	1.203 ± 0.017	1.238 ± 0.025	1.276 ± 0.050	1.390 ± 0.051	1.218 ± 0.078	1.296 ± 0.137
-1.60	0.948 ± 0.011	1.004 ± 0.017	1.118 ± 0.021	1.205 ± 0.018	1.269 ± 0.027	1.351 ± 0.053	1.428 ± 0.054	1.300 ± 0.086	1.222 ± 0.149
-1.46	0.964 ± 0.012	1.034 ± 0.018	1.119 ± 0.021	1.197 ± 0.019	1.307 ± 0.029	1.353 ± 0.056	1.478 ± 0.056	1.505 ± 0.102	1.486 ± 0.167
-1.34	0.973 ± 0.013	1.047 ± 0.019	1.171 ± 0.023	1.184 ± 0.019	1.345 ± 0.030	1.494 ± 0.062	1.555 ± 0.060	1.471 ± 0.100	1.499 ± 0.181
-0.92	1.042 ± 0.009	1.110 ± 0.014	1.220 ± 0.018	1.280 ± 0.015	1.417 ± 0.025	1.435 ± 0.048	1.531 ± 0.049	1.623 ± 0.087	1.890 ± 0.173
-0.65	1.063 ± 0.009	1.121 ± 0.014	1.217 ± 0.017	1.313 ± 0.015	1.408 ± 0.024	1.480 ± 0.049	1.549 ± 0.048	1.717 ± 0.090	1.811 ± 0.149
-0.34	1.077 ± 0.010	1.141 ± 0.015	1.232 ± 0.018	1.368 ± 0.016	1.488 ± 0.026	1.604 ± 0.053	1.773 ± 0.054	1.850 ± 0.095	1.899 ± 0.167
0.00	1.102 ± 0.010	1.169 ± 0.016	1.276 ± 0.020	1.418 ± 0.018	1.528 ± 0.027	1.594 ± 0.054	1.775 ± 0.055	1.935 ± 0.100	1.887 ± 0.173
0.34	1.080 ± 0.010	1.147 ± 0.015	1.272 ± 0.019	1.388 ± 0.017	1.472 ± 0.026	1.596 ± 0.053	1.732 ± 0.053	1.767 ± 0.095	1.790 ± 0.155
0.65	1.065 ± 0.009	1.104 ± 0.015	1.204 ± 0.018	1.335 ± 0.016	1.403 ± 0.024	1.531 ± 0.051	1.661 ± 0.051	1.648 ± 0.089	1.656 ± 0.145
0.92	1.039 ± 0.009	1.120 ± 0.014	1.187 ± 0.017	1.286 ± 0.015	1.368 ± 0.024	1.455 ± 0.049	1.588 ± 0.049	1.679 ± 0.089	1.592 ± 0.146
1.34	0.975 ± 0.012	1.057 ± 0.019	1.122 ± 0.023	1.226 ± 0.020	1.262 ± 0.029	1.361 ± 0.059	1.430 ± 0.056	1.277 ± 0.093	1.469 ± 0.164
1.46	0.980 ± 0.012	1.054 ± 0.019	1.153 ± 0.022	1.207 ± 0.019	1.277 ± 0.029	1.319 ± 0.057	1.554 ± 0.059	1.486 ± 0.102	1.314 ± 0.155
1.60	0.957 ± 0.012	1.003 ± 0.017	1.104 ± 0.021	1.199 ± 0.018	1.249 ± 0.027	1.460 ± 0.058	1.435 ± 0.053	1.398 ± 0.091	1.274 ± 0.159
1.76	0.941 ± 0.011	0.998 ± 0.017	1.063 ± 0.019	1.175 ± 0.017	1.232 ± 0.026	1.324 ± 0.052	1.278 ± 0.049	1.234 ± 0.081	1.281 ± 0.142
1.95	0.913 ± 0.010	0.997 ± 0.016	1.062 ± 0.019	1.131 ± 0.016	1.189 ± 0.025	1.194 ± 0.049	1.216 ± 0.045	1.254 ± 0.082	1.177 ± 0.151
2.19	0.894 ± 0.010	0.968 ± 0.016	0.989 ± 0.018	1.052 ± 0.015	1.114 ± 0.023	1.201 ± 0.047	1.198 ± 0.044	1.193 ± 0.075	1.034 ± 0.123
2.46	0.813 ± 0.009	0.841 ± 0.014	0.912 ± 0.017	0.935 ± 0.014	1.020 ± 0.022	0.980 ± 0.041	0.954 ± 0.038	1.048 ± 0.067	0.754 ± 0.098
2.79	0.701 ± 0.008	0.742 ± 0.012	0.760 ± 0.014	0.804 ± 0.012	0.819 ± 0.017	0.847 ± 0.035	0.838 ± 0.032	0.870 ± 0.057	0.574 ± 0.071
3.19	0.552 ± 0.007	0.579 ± 0.010	0.594 ± 0.011	0.581 ± 0.009	0.586 ± 0.013	0.505 ± 0.024	0.577 ± 0.025	0.561 ± 0.042	0.524 ± 0.069
3.65	0.405 ± 0.006	0.395 ± 0.008	0.401 ± 0.009	0.405 ± 0.008	0.385 ± 0.011	0.399 ± 0.022	0.338 ± 0.020	0.349 ± 0.033	0.413 ± 0.064
4.20	0.220 ± 0.003	0.214 ± 0.004	0.215 ± 0.005	0.196 ± 0.004	0.192 ± 0.006	0.173 ± 0.011	0.156 ± 0.009	0.163 ± 0.018	0.126 ± 0.022
4.74	0.098 ± 0.002	0.097 ± 0.003	0.088 ± 0.003	0.081 ± 0.002	0.072 ± 0.003	0.066 ± 0.007	0.062 ± 0.006	0.059 ± 0.010	0.058 ± 0.015
Toward hemisphere $dN/d\eta$									
-4.74	0.095 ± 0.002	0.088 ± 0.003	0.081 ± 0.003	0.072 ± 0.002	0.069 ± 0.003	0.056 ± 0.006	0.074 ± 0.006	0.053 ± 0.008	0.038 ± 0.011
-4.20	0.222 ± 0.003	0.208 ± 0.005	0.201 ± 0.005	0.199 ± 0.004	0.182 ± 0.006	0.178 ± 0.011	0.158 ± 0.010	0.179 ± 0.019	0.127 ± 0.024
-3.65	0.394 ± 0.005	0.366 ± 0.008	0.346 ± 0.008	0.350 ± 0.007	0.333 ± 0.010	0.319 ± 0.018	0.305 ± 0.017	0.326 ± 0.030	0.282 ± 0.049
-3.19	0.541 ± 0.006	0.531 ± 0.009	0.511 ± 0.009	0.521 ± 0.008	0.490 ± 0.011	0.486 ± 0.021	0.497 ± 0.021	0.440 ± 0.034	0.427 ± 0.055
-2.79	0.699 ± 0.008	0.664 ± 0.011	0.672 ± 0.012	0.690 ± 0.010	0.660 ± 0.014	0.652 ± 0.028	0.678 ± 0.027	0.756 ± 0.051	0.733 ± 0.083
-2.46	0.815 ± 0.009	0.794 ± 0.013	0.785 ± 0.015	0.816 ± 0.012	0.800 ± 0.018	0.850 ± 0.035	0.776 ± 0.032	0.745 ± 0.054	0.840 ± 0.098
-2.19	0.869 ± 0.010	0.845 ± 0.015	0.856 ± 0.017	0.865 ± 0.014	0.876 ± 0.020	0.869 ± 0.037	0.864 ± 0.036	0.834 ± 0.060	0.915 ± 0.109
-1.95	0.938 ± 0.012	0.875 ± 0.016	0.924 ± 0.018	0.949 ± 0.016	0.947 ± 0.022	1.012 ± 0.045	0.981 ± 0.041	0.950 ± 0.070	0.862 ± 0.116
-1.76	0.948 ± 0.012	0.905 ± 0.016	0.940 ± 0.018	0.966 ± 0.016	0.978 ± 0.023	0.919 ± 0.041	0.966 ± 0.041	0.906 ± 0.069	0.959 ± 0.128
-1.60	0.948 ± 0.012	0.919 ± 0.017	0.930 ± 0.019	0.959 ± 0.016	0.909 ± 0.023	0.967 ± 0.045	0.986 ± 0.042	1.002 ± 0.079	0.943 ± 0.119
-1.46	0.964 ± 0.013	0.957 ± 0.019	0.965 ± 0.021	0.994 ± 0.018	1.030 ± 0.028	0.971 ± 0.048	1.063 ± 0.047	1.134 ± 0.089	0.667 ± 0.101
-1.34	0.973 ± 0.014	0.937 ± 0.019	0.945 ± 0.022	1.035 ± 0.019	1.050 ± 0.026	1.007 ± 0.051	1.022 ± 0.049	1.073 ± 0.090	1.021 ± 0.150
-0.92	1.042 ± 0.017	0.973 ± 0.021	1.067 ± 0.025	1.075 ± 0.021	1.101 ± 0.030	1.058 ± 0.054	1.139 ± 0.053	0.971 ± 0.087	1.151 ± 0.156
-0.65	1.063 ± 0.017	1.030 ± 0.022	1.132 ± 0.026	1.154 ± 0.022	1.186 ± 0.031	1.082 ± 0.055	1.217 ± 0.055	1.127 ± 0.090	1.214 ± 0.156
-0.34	1.077 ± 0.017	1.132 ± 0.023	1.243 ± 0.027	1.237 ± 0.023	1.288 ± 0.032	1.332 ± 0.060	1.259 ± 0.055	1.363 ± 0.098	1.541 ± 0.179
0.00	1.102 ± 0.016	1.131 ± 0.022	1.226 ± 0.026	1.242 ± 0.022	1.278 ± 0.031	1.226 ± 0.057	1.316 ± 0.056	1.204 ± 0.092	1.397 ± 0.173
0.34	1.080 ± 0.016	1.118 ± 0.022	1.185 ± 0.025	1.213 ± 0.022	1.268 ± 0.031	1.334 ± 0.060	1.286 ± 0.054	1.313 ± 0.094	1.323 ± 0.160
0.65	1.065 ± 0.017	1.095 ± 0.023	1.130 ± 0.026	1.189 ± 0.022	1.184 ± 0.031	1.213 ± 0.057	1.229 ± 0.055	1.255 ± 0.095	1.252 ± 0.157
0.92	1.039 ± 0.017	0.983 ± 0.021	1.031 ± 0.025	1.082 ± 0.021	1.121 ± 0.030	1.085 ± 0.055	1.134 ± 0.053	1.145 ± 0.093	1.007 ± 0.143
1.34	0.975 ± 0.014	0.921 ± 0.019	0.971 ± 0.022	0.987 ± 0.019	0.973 ± 0.026	1.008 ± 0.052	0.995 ± 0.049	1.067 ± 0.088	0.717 ± 0.118
1.46	0.980 ± 0.013	0.971 ± 0.019	0.961 ± 0.021	0.926 ± 0.018	0.978 ± 0.025	1.003 ± 0.047	1.064 ± 0.047	0.935 ± 0.074	0.808 ± 0.118
1.60	0.957 ± 0.012	0.922 ± 0.017	0.987 ± 0.023	0.940 ± 0.016	0.955 ± 0.023	0.971 ± 0.046	0.962 ± 0.043	0.974 ± 0.074	0.844 ± 0.125
1.76	0.941 ± 0.011	0.902 ± 0.016	0.933 ± 0.019	0.921 ± 0.016	0.941 ± 0.023	0.956 ± 0.043	0.954 ± 0.041	1.064 ± 0.074	0.763 ± 0.107
1.95	0.913 ± 0.012	0.885 ± 0.016	0.889 ± 0.018	0.900 ± 0.015	0.906 ± 0.022	0.916 ± 0.042	0.884 ± 0.039	0.875 ± 0.067	0.862 ± 0.112
2.19	0.894 ± 0.010	0.861 ± 0.015	0.863 ± 0.017	0.848 ± 0.013	0.846 ± 0.020	0.860 ± 0.038	0.899 ± 0.038	0.956 ± 0.067	0.881 ± 0.111
2.46	0.814 ± 0.009	0.786 ± 0.013	0.790 ± 0.015	0.793 ± 0.012	0.802 ± 0.018	0.798 ± 0.035	0.779 ± 0.032	0.809 ± 0.056	0.835 ± 0.099
2.79	0.701 ± 0.008	0.686 ± 0.011	0.664 ± 0.012	0.680 ± 0.010	0.668 ± 0.015	0.663 ± 0.028	0.657 ± 0.026	0.692 ± 0.048	0.665 ± 0.079
3.19	0.552 ± 0.006	0.514 ± 0.008	0.516 ± 0.010	0.501 ± 0.008	0.502 ± 0.012	0.516 ± 0.023	0.492 ± 0.021	0.471 ± 0.036	0.475 ± 0.058
3.65	0.405 ± 0.006	0.364 ± 0.008	0.368 ± 0.009	0.356 ± 0.007	0.332 ± 0.010	0.328 ± 0.019	0.307 ± 0.018	0.288 ± 0.030	0.266 ± 0.047
4.20	0.220 ± 0.003	0.208 ± 0.004	0.196 ± 0.005	0.179 ± 0.004	0.175 ± 0.005	0.170 ± 0.011	0.152 ± 0.009	0.160 ± 0.016	0.178 ± 0.029
4.74	0.097 ± 0.002	0.090 ± 0.003	0.088 ± 0.003	0.078 ± 0.002	0.075 ± 0.003	0.078 ± 0.007	0.056 ± 0.005	0.052 ± 0.005	0.039 ± 0.011

events,

B. the high- p_{\perp} trigger particle itself (here a photon) plus any accompanying particles nearby in solid angle, and

C. a collection of particles whose origin is closely connected with B , and whose transverse momentum approximately balances that of the trigger particle (B).

We assume that components A , B , and C add incoherently to yield the total observed multiplicity. The B and C components correspond, in hard-scattering models, to the “alongside” and “away” jets predicted to arise from final-state interactions of the scattered constituents. However, the extent to which particle production may be factored into these three components can be discussed

without reference to specific models; thus, we refrain from attaching names to these components which suggest a bias toward any particular model for production.

In order to proceed to a quantitative discussion of the C component and its dependence on p_{\perp} and \sqrt{s} , we make several assumptions appropriate to the data with a photon near $\theta = 90^\circ$:

- (i) The number of charged particles accompanying the photon trigger (the B component) is negligible. This is borne out by recent measurements of alongside correlations.⁵ Physically, it arises because of the bias imposed against having several high- p_{\perp} particles close to each other, due to the requirement of observing a single high- p_{\perp} photon.
- (ii) The particles in the C component are en-

TABLE V. Differential multiplicity distributions for away and toward hemispheres. Photon detector is at 17.5° , and $\sqrt{s} = 23$ GeV.

Away hemisphere $dN/d\eta$						
η	p_{\perp} (GeV/c) 0.0-0.5	p_{\perp} (GeV/c) 0.5-1.0	p_{\perp} (GeV/c) 1.0-1.5	p_{\perp} (GeV/c) 1.5-2.0	p_{\perp} (GeV/c) 2.0-2.5	p_{\perp} (GeV/c) 2.5-3.0
-4.74	0.076 ± 0.001	0.076 ± 0.002	0.070 ± 0.002	0.058 ± 0.007	0.053 ± 0.021	0.332 ± 0.171
-4.20	0.172 ± 0.002	0.171 ± 0.003	0.157 ± 0.003	0.137 ± 0.010	0.137 ± 0.037	0.003 ± 0.000
-3.65	0.346 ± 0.004	0.358 ± 0.005	0.353 ± 0.007	0.342 ± 0.021	0.356 ± 0.083	0.001 ± 0.000
-3.19	0.647 ± 0.006	0.689 ± 0.008	0.723 ± 0.011	0.744 ± 0.034	0.805 ± 0.129	0.724 ± 0.398
-2.79	0.875 ± 0.008	0.906 ± 0.011	0.981 ± 0.013	1.085 ± 0.045	1.078 ± 0.151	1.784 ± 0.528
-2.46	1.062 ± 0.009	1.111 ± 0.012	1.171 ± 0.016	1.271 ± 0.052	1.467 ± 0.189	2.734 ± 0.928
-2.19	1.229 ± 0.010	1.262 ± 0.014	1.312 ± 0.017	1.517 ± 0.059	1.533 ± 0.217	1.091 ± 0.402
-1.95	1.380 ± 0.011	1.435 ± 0.016	1.565 ± 0.020	1.602 ± 0.064	1.431 ± 0.196	5.167 ± 2.063
-1.76	1.467 ± 0.012	1.531 ± 0.017	1.650 ± 0.021	1.662 ± 0.067	2.280 ± 0.297	2.701 ± 1.258
-1.60	1.520 ± 0.013	1.606 ± 0.018	1.653 ± 0.022	1.846 ± 0.075	2.038 ± 0.304	2.162 ± 1.196
-1.46	1.549 ± 0.014	1.625 ± 0.019	1.727 ± 0.024	1.948 ± 0.081	1.790 ± 0.271	1.668 ± 0.587
-1.34	1.562 ± 0.014	1.679 ± 0.020	1.786 ± 0.026	1.878 ± 0.082	1.833 ± 0.302	2.782 ± 1.510
-0.92	1.577 ± 0.011	1.655 ± 0.016	1.814 ± 0.020	1.979 ± 0.067	2.335 ± 0.273	0.972 ± 0.433
-0.65	1.598 ± 0.011	1.661 ± 0.015	1.830 ± 0.020	2.024 ± 0.067	2.566 ± 0.304	2.917 ± 0.530
-0.34	1.599 ± 0.011	1.694 ± 0.015	1.821 ± 0.020	2.030 ± 0.067	2.614 ± 0.264	2.716 ± 0.697
0.00	1.659 ± 0.011	1.729 ± 0.016	1.848 ± 0.020	2.089 ± 0.067	2.518 ± 0.263	2.695 ± 1.209
0.34	1.683 ± 0.011	1.731 ± 0.016	1.891 ± 0.020	2.082 ± 0.067	2.378 ± 0.249	2.006 ± 0.629
0.65	1.796 ± 0.012	1.810 ± 0.017	1.977 ± 0.021	2.230 ± 0.071	2.112 ± 0.250	2.244 ± 0.847
0.92	1.905 ± 0.013	1.901 ± 0.017	2.007 ± 0.022	1.987 ± 0.065	2.309 ± 0.266	6.100 ± 1.016
1.34	2.066 ± 0.019	1.981 ± 0.023	1.943 ± 0.027	2.024 ± 0.084	2.652 ± 0.341	3.069 ± 1.615
1.46	2.084 ± 0.018	2.014 ± 0.022	1.992 ± 0.026	1.974 ± 0.076	1.743 ± 0.286	1.901 ± 0.014
1.60	2.082 ± 0.018	2.008 ± 0.022	1.931 ± 0.025	1.767 ± 0.072	1.751 ± 0.263	0.132 ± 0.001
1.76	2.074 ± 0.018	1.963 ± 0.022	1.838 ± 0.025	1.899 ± 0.077	1.419 ± 0.234	1.561 ± 0.778
1.95	1.974 ± 0.017	1.840 ± 0.021	1.690 ± 0.023	1.618 ± 0.069	1.177 ± 0.203	1.480 ± 0.765
2.19	1.698 ± 0.014	1.589 ± 0.017	1.398 ± 0.019	1.259 ± 0.054	0.751 ± 0.141	0.064 ± 0.000
2.46	1.372 ± 0.011	1.305 ± 0.014	1.100 ± 0.015	0.892 ± 0.042	0.791 ± 0.137	1.003 ± 0.379
2.79	1.075 ± 0.009	1.004 ± 0.011	0.850 ± 0.012	0.668 ± 0.034	0.787 ± 0.136	0.008 ± 0.000
3.19	0.727 ± 0.007	0.634 ± 0.008	0.500 ± 0.008	0.311 ± 0.021	0.426 ± 0.092	0.348 ± 0.261
3.65	0.306 ± 0.003	0.259 ± 0.004	0.181 ± 0.004	0.133 ± 0.013	0.043 ± 0.027	0.005 ± 0.000
4.20	0.119 ± 0.001	0.097 ± 0.002	0.069 ± 0.002	0.053 ± 0.006	0.013 ± 0.011	0.002 ± 0.000
4.74	0.045 ± 0.001	0.036 ± 0.001	0.024 ± 0.001	0.021 ± 0.004	0.032 ± 0.021	0.002 ± 0.000
Toward hemisphere $dN/d\eta$						
-4.74	0.076 ± 0.001	0.074 ± 0.002	0.065 ± 0.002	0.061 ± 0.007	0.045 ± 0.022	0.164 ± 0.117
-4.20	0.172 ± 0.002	0.167 ± 0.003	0.152 ± 0.003	0.138 ± 0.010	0.175 ± 0.038	0.324 ± 0.167
-3.65	0.346 ± 0.004	0.327 ± 0.005	0.302 ± 0.006	0.279 ± 0.019	0.318 ± 0.078	1.450 ± 0.662
-3.19	0.647 ± 0.006	0.616 ± 0.008	0.592 ± 0.009	0.551 ± 0.028	0.542 ± 0.098	0.344 ± 0.253
-2.79	0.875 ± 0.007	0.859 ± 0.010	0.822 ± 0.012	0.788 ± 0.036	0.827 ± 0.137	0.811 ± 0.308
-2.46	1.062 ± 0.009	1.012 ± 0.012	0.998 ± 0.014	0.933 ± 0.044	0.863 ± 0.143	0.900 ± 0.504
-2.19	1.229 ± 0.011	1.170 ± 0.014	1.180 ± 0.017	1.212 ± 0.053	1.425 ± 0.210	0.964 ± 0.553
-1.95	1.380 ± 0.012	1.320 ± 0.016	1.280 ± 0.019	1.315 ± 0.061	1.136 ± 0.211	0.447 ± 0.405
-1.76	1.467 ± 0.013	1.416 ± 0.017	1.355 ± 0.020	1.449 ± 0.064	1.581 ± 0.230	0.556 ± 0.442
-1.60	1.520 ± 0.014	1.435 ± 0.018	1.450 ± 0.021	1.398 ± 0.066	1.376 ± 0.218	0.615 ± 0.481
-1.46	1.549 ± 0.015	1.443 ± 0.019	1.413 ± 0.022	1.395 ± 0.069	0.754 ± 0.190	1.475 ± 0.817
-1.34	1.562 ± 0.014	1.460 ± 0.020	1.386 ± 0.023	1.548 ± 0.078	0.668 ± 0.194	0.724 ± 0.608
-0.92	1.577 ± 0.015	1.479 ± 0.019	1.473 ± 0.023	1.520 ± 0.074	1.869 ± 0.283	0.390 ± 0.003
-0.65	1.598 ± 0.015	1.465 ± 0.019	1.422 ± 0.022	1.423 ± 0.070	1.393 ± 0.226	1.411 ± 0.472
-0.34	1.599 ± 0.014	1.425 ± 0.018	1.367 ± 0.021	1.371 ± 0.065	1.025 ± 0.211	2.640 ± 0.709
0.00	1.659 ± 0.015	1.445 ± 0.018	1.360 ± 0.021	1.449 ± 0.068	1.017 ± 0.214	0.184 ± 0.376
0.34	1.683 ± 0.015	1.392 ± 0.017	1.302 ± 0.020	1.226 ± 0.062	1.253 ± 0.229	0.687 ± 0.562
0.65	1.796 ± 0.016	1.444 ± 0.018	1.340 ± 0.021	1.300 ± 0.068	1.231 ± 0.239	0.717 ± 0.437
0.92	1.905 ± 0.018	1.537 ± 0.020	1.354 ± 0.023	1.267 ± 0.071	0.801 ± 0.229	0.081 ± 0.446
1.34	2.066 ± 0.020	1.753 ± 0.024	1.471 ± 0.025	1.435 ± 0.080	1.497 ± 0.297	0.219 ± 0.002
1.46	2.084 ± 0.020	1.829 ± 0.023	1.523 ± 0.025	1.330 ± 0.075	1.188 ± 0.249	1.391 ± 0.856
1.60	2.082 ± 0.018	1.798 ± 0.021	1.520 ± 0.023	1.244 ± 0.075	1.429 ± 0.243	1.358 ± 0.778
1.76	2.074 ± 0.018	1.737 ± 0.020	1.405 ± 0.021	1.099 ± 0.058	1.247 ± 0.231	1.657 ± 0.005
1.95	1.974 ± 0.017	1.581 ± 0.019	1.271 ± 0.020	1.028 ± 0.056	0.872 ± 0.191	0.571 ± 0.485
2.19	1.698 ± 0.014	1.398 ± 0.016	1.084 ± 0.016	0.801 ± 0.044	0.838 ± 0.155	1.045 ± 0.425
2.46	1.372 ± 0.011	1.125 ± 0.013	0.795 ± 0.012	0.607 ± 0.035	0.590 ± 0.122	0.027 ± 0.000
2.79	1.075 ± 0.009	0.796 ± 0.010	0.590 ± 0.009	0.482 ± 0.027	0.350 ± 0.083	0.008 ± 0.000
3.19	0.727 ± 0.007	0.496 ± 0.007	0.351 ± 0.007	0.267 ± 0.019	0.191 ± 0.062	0.351 ± 0.257
3.65	0.306 ± 0.003	0.211 ± 0.004	0.144 ± 0.004	0.105 ± 0.011	0.054 ± 0.027	0.005 ± 0.000
4.20	0.119 ± 0.001	0.088 ± 0.002	0.066 ± 0.002	0.045 ± 0.005	0.018 ± 0.011	0.002 ± 0.000
4.74	0.045 ± 0.001	0.032 ± 0.001	0.026 ± 0.001	0.018 ± 0.003	0.019 ± 0.017	0.002 ± 0.000

tirely contained within the hemisphere away from the trigger photon. Our observation of the azimuthal width of the excess multiplicity (Fig. 10) supports this assumption. We assume that the particles in the C component share equally in balancing the p_{\perp} of the photon.

(iii) The particles in the A component are assumed to be distributed in angle in the same way as those particles actually observed in ordinary low- p_{\perp} collisions at a reduced c.m. energy, $\sqrt{s}_R = \sqrt{s} - E_B - E_C$. Here E_B and E_C are the energies removed from the total by the B and C components. We note that the A -component multiplicities are observed⁹ to be azimuthally symmetric; thus, the A component is identical in away and toward

hemispheres.

Under assumptions (i) and (ii), the reduced energy is given by

$$\sqrt{s}_R = \sqrt{s} - p_{\perp} - p_{\perp} \langle 1/\sin\theta \rangle_C,$$

where we assume that the masses are small compared to the momenta involved, and $\langle 1/\sin\theta \rangle_C$ is obtained by averaging over the C component. This angular factor is determined from the results of our analysis (Fig. 16). We have verified that the results are insensitive to the details of the assumed sharing of transverse momentum in the C component.

The expected charged multiplicity associated with a photon of transverse momentum p_{\perp} pro-

TABLE VI. Differential multiplicity distributions for away and toward hemispheres. Photon detector is at 17.5° , and $\sqrt{s} = 53$ GeV.

η	Away hemisphere $dN/d\eta$								
	p_{\perp} (GeV/c) 0.0-0.5	p_{\perp} (GeV/c) 0.5-1.0	p_{\perp} (GeV/c) 1.0-1.5	p_{\perp} (GeV/c) 1.5-2.0	p_{\perp} (GeV/c) 2.0-2.5	p_{\perp} (GeV/c) 2.5-3.0	p_{\perp} (GeV/c) 3.0-3.5	p_{\perp} (GeV/c) 3.5-4.0	p_{\perp} (GeV/c) 4.0-4.5
-4.74	0.228 ± 0.002	0.232 ± 0.003	0.219 ± 0.003	0.207 ± 0.003	0.199 ± 0.003	0.185 ± 0.005	0.179 ± 0.010	0.187 ± 0.020	0.119 ± 0.032
-4.20	0.472 ± 0.004	0.471 ± 0.005	0.492 ± 0.005	0.475 ± 0.005	0.479 ± 0.005	0.459 ± 0.008	0.445 ± 0.016	0.394 ± 0.030	0.461 ± 0.065
-3.65	0.781 ± 0.007	0.818 ± 0.009	0.829 ± 0.009	0.836 ± 0.010	0.859 ± 0.010	0.871 ± 0.015	0.823 ± 0.029	0.883 ± 0.062	0.834 ± 0.120
-3.19	1.025 ± 0.007	1.082 ± 0.010	1.112 ± 0.010	1.145 ± 0.011	1.184 ± 0.011	1.181 ± 0.017	1.177 ± 0.032	1.243 ± 0.071	1.505 ± 0.157
-2.79	1.258 ± 0.009	1.315 ± 0.012	1.389 ± 0.012	1.435 ± 0.013	1.523 ± 0.013	1.554 ± 0.020	1.559 ± 0.040	1.742 ± 0.088	1.648 ± 0.167
-2.46	1.417 ± 0.010	1.481 ± 0.013	1.582 ± 0.014	1.668 ± 0.015	1.748 ± 0.015	1.794 ± 0.023	1.836 ± 0.046	2.042 ± 0.106	1.990 ± 0.194
-2.19	1.491 ± 0.010	1.563 ± 0.014	1.680 ± 0.015	1.787 ± 0.016	1.888 ± 0.016	1.921 ± 0.025	2.080 ± 0.052	2.165 ± 0.108	2.509 ± 0.238
-1.95	1.543 ± 0.010	1.633 ± 0.014	1.742 ± 0.016	1.842 ± 0.017	1.969 ± 0.017	2.059 ± 0.026	2.169 ± 0.053	2.135 ± 0.109	2.866 ± 0.268
-1.76	1.554 ± 0.011	1.643 ± 0.015	1.818 ± 0.017	1.928 ± 0.018	2.054 ± 0.018	2.190 ± 0.028	2.377 ± 0.058	2.522 ± 0.126	2.695 ± 0.255
-1.60	1.549 ± 0.011	1.648 ± 0.015	1.782 ± 0.017	1.917 ± 0.018	2.021 ± 0.019	2.182 ± 0.029	2.321 ± 0.059	2.467 ± 0.125	2.716 ± 0.273
-1.46	1.549 ± 0.012	1.648 ± 0.016	1.811 ± 0.018	1.931 ± 0.019	2.107 ± 0.020	2.227 ± 0.031	2.432 ± 0.064	2.591 ± 0.138	2.978 ± 0.306
-1.34	1.538 ± 0.012	1.630 ± 0.017	1.801 ± 0.018	1.932 ± 0.020	2.112 ± 0.021	2.215 ± 0.032	2.365 ± 0.065	2.449 ± 0.136	2.880 ± 0.290
-0.92	1.546 ± 0.009	1.631 ± 0.013	1.790 ± 0.014	1.929 ± 0.016	2.088 ± 0.021	2.255 ± 0.026	2.417 ± 0.053	2.507 ± 0.116	3.118 ± 0.277
-0.65	1.550 ± 0.009	1.657 ± 0.013	1.805 ± 0.014	1.983 ± 0.016	2.135 ± 0.016	2.376 ± 0.027	2.554 ± 0.055	2.701 ± 0.117	2.438 ± 0.223
-0.34	1.540 ± 0.010	1.665 ± 0.013	1.827 ± 0.015	2.021 ± 0.016	2.193 ± 0.017	2.386 ± 0.027	2.653 ± 0.056	2.712 ± 0.117	2.571 ± 0.226
0.00	1.596 ± 0.010	1.697 ± 0.014	1.885 ± 0.015	2.074 ± 0.017	2.300 ± 0.018	2.452 ± 0.028	2.579 ± 0.055	2.629 ± 0.114	3.231 ± 0.270
0.34	1.642 ± 0.010	1.748 ± 0.014	1.898 ± 0.015	2.104 ± 0.017	2.300 ± 0.018	2.490 ± 0.028	2.568 ± 0.055	2.996 ± 0.124	3.052 ± 0.250
0.65	1.721 ± 0.011	1.798 ± 0.014	1.958 ± 0.016	2.127 ± 0.017	2.349 ± 0.018	2.497 ± 0.028	2.591 ± 0.055	2.625 ± 0.114	3.233 ± 0.263
0.92	1.847 ± 0.011	1.924 ± 0.015	2.052 ± 0.016	2.235 ± 0.018	2.381 ± 0.018	2.481 ± 0.028	2.584 ± 0.056	2.625 ± 0.117	2.597 ± 0.237
1.34	2.027 ± 0.016	2.071 ± 0.021	2.167 ± 0.022	2.274 ± 0.023	2.393 ± 0.023	2.434 ± 0.035	2.416 ± 0.066	2.258 ± 0.130	2.354 ± 0.268
1.46	2.047 ± 0.016	2.095 ± 0.020	2.182 ± 0.021	2.260 ± 0.022	2.363 ± 0.022	2.372 ± 0.032	2.323 ± 0.066	2.233 ± 0.118	2.016 ± 0.227
1.60	2.094 ± 0.016	2.132 ± 0.020	2.172 ± 0.021	2.258 ± 0.022	2.355 ± 0.022	2.379 ± 0.032	2.293 ± 0.060	2.174 ± 0.119	2.693 ± 0.296
1.76	2.126 ± 0.016	2.135 ± 0.020	2.214 ± 0.021	2.285 ± 0.022	2.360 ± 0.022	2.353 ± 0.032	2.237 ± 0.059	2.313 ± 0.123	2.287 ± 0.230
1.95	2.200 ± 0.017	2.168 ± 0.021	2.175 ± 0.021	2.262 ± 0.022	2.298 ± 0.022	2.264 ± 0.032	2.204 ± 0.060	2.065 ± 0.119	1.884 ± 0.223
2.19	2.072 ± 0.015	2.047 ± 0.018	2.052 ± 0.018	2.059 ± 0.018	2.058 ± 0.018	1.999 ± 0.027	1.880 ± 0.050	1.556 ± 0.092	1.162 ± 0.144
2.46	1.892 ± 0.013	1.831 ± 0.016	1.833 ± 0.016	1.829 ± 0.017	1.786 ± 0.016	1.653 ± 0.023	1.464 ± 0.040	1.314 ± 0.079	1.143 ± 0.155
2.79	1.609 ± 0.011	1.511 ± 0.013	1.493 ± 0.013	1.451 ± 0.013	1.374 ± 0.012	1.249 ± 0.018	1.136 ± 0.033	0.947 ± 0.062	0.925 ± 0.123
3.19	1.227 ± 0.008	1.125 ± 0.010	1.075 ± 0.010	1.015 ± 0.010	0.938 ± 0.009	0.845 ± 0.013	0.751 ± 0.024	0.593 ± 0.044	0.484 ± 0.076
3.65	0.819 ± 0.007	0.752 ± 0.008	0.715 ± 0.008	0.624 ± 0.008	0.560 ± 0.007	0.483 ± 0.010	0.408 ± 0.018	0.317 ± 0.035	0.353 ± 0.072
4.20	0.425 ± 0.003	0.394 ± 0.004	0.368 ± 0.004	0.320 ± 0.004	0.270 ± 0.003	0.231 ± 0.005	0.180 ± 0.009	0.163 ± 0.017	0.134 ± 0.039
4.74	0.168 ± 0.002	0.154 ± 0.003	0.130 ± 0.002	0.104 ± 0.002	0.083 ± 0.002	0.072 ± 0.003	0.051 ± 0.005	0.037 ± 0.008	0.059 ± 0.020
η	Toward hemisphere $dN/d\eta$								
	p_{\perp} (GeV/c) 0.0-0.5	p_{\perp} (GeV/c) 0.5-1.0	p_{\perp} (GeV/c) 1.0-1.5	p_{\perp} (GeV/c) 1.5-2.0	p_{\perp} (GeV/c) 2.0-2.5	p_{\perp} (GeV/c) 2.5-3.0	p_{\perp} (GeV/c) 3.0-3.5	p_{\perp} (GeV/c) 3.5-4.0	p_{\perp} (GeV/c) 4.0-4.5
-4.74	0.228 ± 0.002	0.209 ± 0.003	0.205 ± 0.003	0.194 ± 0.003	0.180 ± 0.003	0.168 ± 0.004	0.188 ± 0.010	0.174 ± 0.018	0.106 ± 0.031
-4.20	0.472 ± 0.004	0.450 ± 0.005	0.440 ± 0.005	0.428 ± 0.005	0.411 ± 0.005	0.405 ± 0.008	0.384 ± 0.015	0.392 ± 0.031	0.272 ± 0.054
-3.65	0.781 ± 0.006	0.754 ± 0.008	0.753 ± 0.008	0.745 ± 0.009	0.719 ± 0.008	0.711 ± 0.012	0.634 ± 0.023	0.661 ± 0.049	0.680 ± 0.094
-3.19	1.025 ± 0.007	1.006 ± 0.009	1.013 ± 0.009	1.019 ± 0.009	0.989 ± 0.009	0.968 ± 0.013	0.960 ± 0.027	1.000 ± 0.056	1.125 ± 0.122
-2.79	1.258 ± 0.008	1.266 ± 0.011	1.252 ± 0.011	1.267 ± 0.011	1.260 ± 0.011	1.282 ± 0.017	1.277 ± 0.033	1.322 ± 0.071	1.362 ± 0.146
-2.46	1.417 ± 0.010	1.396 ± 0.013	1.424 ± 0.013	1.452 ± 0.014	1.464 ± 0.013	1.453 ± 0.020	1.479 ± 0.040	1.595 ± 0.085	1.171 ± 0.146
-2.19	1.491 ± 0.010	1.489 ± 0.014	1.509 ± 0.014	1.571 ± 0.015	1.579 ± 0.014	1.582 ± 0.022	1.525 ± 0.043	1.651 ± 0.093	1.945 ± 0.198
-1.95	1.543 ± 0.011	1.520 ± 0.015	1.582 ± 0.015	1.621 ± 0.016	1.663 ± 0.016	1.649 ± 0.024	1.622 ± 0.047	1.717 ± 0.102	2.263 ± 0.243
-1.76	1.554 ± 0.011	1.541 ± 0.015	1.586 ± 0.015	1.620 ± 0.016	1.647 ± 0.016	1.689 ± 0.024	1.644 ± 0.047	1.600 ± 0.097	1.743 ± 0.182
-1.60	1.549 ± 0.012	1.519 ± 0.015	1.568 ± 0.016	1.623 ± 0.017	1.632 ± 0.016	1.653 ± 0.025	1.633 ± 0.049	1.748 ± 0.105	1.649 ± 0.202
-1.46	1.549 ± 0.013	1.502 ± 0.016	1.579 ± 0.017	1.603 ± 0.018	1.669 ± 0.017	1.661 ± 0.027	1.665 ± 0.053	1.751 ± 0.113	1.747 ± 0.220
-1.34	1.538 ± 0.013	1.509 ± 0.017	1.587 ± 0.018	1.655 ± 0.019	1.683 ± 0.018	1.656 ± 0.028	1.613 ± 0.054	1.809 ± 0.116	1.691 ± 0.234
-0.92	1.546 ± 0.013	1.513 ± 0.017	1.567 ± 0.017	1.651 ± 0.018	1.705 ± 0.018	1.774 ± 0.028	1.744 ± 0.054	1.980 ± 0.120	2.111 ± 0.227
-0.65	1.550 ± 0.013	1.493 ± 0.016	1.573 ± 0.017	1.664 ± 0.018	1.682 ± 0.018	1.716 ± 0.027	1.775 ± 0.054	1.799 ± 0.112	1.642 ± 0.216
-0.34	1.540 ± 0.012	1.481 ± 0.016	1.545 ± 0.016	1.601 ± 0.017	1.668 ± 0.017	1.663 ± 0.026	1.637 ± 0.050	1.610 ± 0.098	1.798 ± 0.219
0.00	1.596 ± 0.013	1.502 ± 0.016	1.592 ± 0.017	1.616 ± 0.017	1.691 ± 0.017	1.672 ± 0.025	1.690 ± 0.051	1.591 ± 0.099	1.511 ± 0.186
0.34	1.642 ± 0.013	1.511 ± 0.016	1.571 ± 0.016	1.609 ± 0.017	1.693 ± 0.017	1.683 ± 0.026	1.639 ± 0.050	1.687 ± 0.107	1.647 ± 0.201
0.65	1.721 ± 0.014	1.583 ± 0.017	1.638 ± 0.017	1.672 ± 0.018	1.726 ± 0.018	1.706 ± 0.027	1.628 ± 0.051	1.452 ± 0.104	1.887 ± 0.234
0.92	1.847 ± 0.016	1.704 ± 0.019	1.702 ± 0.019	1.756 ± 0.020	1.771 ± 0.019	1.720 ± 0.029	1.583 ± 0.054	1.645 ± 0.116	1.726 ± 0.235
1.34	2.027 ± 0.017	1.952 ± 0.021	1.916 ± 0.021	1.912 ± 0.022	1.890 ± 0.021	1.797 ± 0.030	1.679 ± 0.057	1.578 ± 0.115	1.470 ± 0.210
1.46	2.047 ± 0.017	2.010 ± 0.021	1.944 ± 0.020	1.886 ± 0.021	1.857 ± 0.019	1.820 ± 0.029	1.629 ± 0.054	1.628 ± 0.119	1.839 ± 0.246
1.60	2.094 ± 0.016	2.062 ± 0.020	2.014 ± 0.020	1.952 ± 0.020	1.875 ± 0.019	1.827 ± 0.027	1.803 ± 0.053	1.577 ± 0.104	1.752 ± 0.198
1.76	2.126 ± 0.016	2.065 ± 0.019	1.946 ± 0.019	1.911 ± 0.019	1.805 ± 0.017	1.703 ± 0.025	1.658 ± 0.050	1.455 ± 0.095	1.439 ± 0.179
1.95	2.200 ± 0.016	2.089 ± 0.019	1.933 ± 0.019	1.865 ± 0.019	1.777 ± 0.017	1.712 ± 0.026	1.646 ± 0.049	1.482 ± 0.096	1.114 ± 0.158
2.19	2.072 ± 0.014	1.995 ± 0.017	1.813 ± 0.016	1.745 ± 0.016	1.621 ± 0.015	1.530 ± 0.022	1.459 ± 0.042	1.418 ± 0.086	0.904 ± 0.139
2.46	1.892 ± 0.013	1.745 ± 0.015	1.597 ± 0.014	1.505 ± 0.014	1.380 ± 0.013	1.275 ± 0.018	1.183 ± 0.035	1.030 ± 0.068	1.020 ± 0.134
2.79	1.609 ± 0.010	1.416 ± 0.012	1.245 ± 0.011	1.169 ± 0.010	1.053 ± 0.009	0.969 ± 0.014	0.881 ± 0.027	0.761 ± 0.051	0.705 ± 0.090
3.19	1.227 ± 0.008	1.004 ± 0.009	0.869 ± 0.008	0.781 ± 0.008	0.688 ± 0.007	0.626 ± 0.010	0.520 ± 0.018	0.530 ± 0.040	0.436 ± 0.072
3.65	0.819 ± 0.006	0.660 ± 0.007	0.549 ± 0.006	0.503 ± 0.006	0.426 ± 0.005	0.366 ± 0.008	0.334 ± 0.016	0.302 ± 0.031	0.208 ± 0.055
4.20	0.425 ± 0.003	0.349 ± 0.004	0.297 ± 0.004	0.258 ± 0.003	0.211 ± 0.003	0.188 ± 0.005	0.159 ± 0.009	0.148 ± 0.017	0.084 ± 0.027
4.74	0.168 ± 0.002	0.142 ± 0.002	0.116 ± 0.002	0.098 ± 0.002	0.082 ± 0.002	0.066 ± 0.002	0.060 ± 0.005	0.077 ± 0.014	0.051 ± 0.019

duced in a collision at energy \sqrt{s} can be written for the away and toward hemispheres:

$$N^{(\text{away})}(\sqrt{s}; p_{\perp}) = N_A(\sqrt{s}_R; \text{low } p_{\perp}) + N_C(\sqrt{s}; p_{\perp}),$$

$$N^{(\text{toward})}(\sqrt{s}; p_{\perp}) = N_A(\sqrt{s}_R; \text{low } p_{\perp}).$$

Subscripts A and C refer to the A and C components, and $N_A(\sqrt{s}; \text{low } p_{\perp})$ is the multiplicity of charged particles produced in *either* hemisphere for normal low- p_{\perp} ($0 \leq p_{\perp} \leq 0.5$ GeV/c) events with a photon produced at $\theta = 90^\circ$. Thus, toward-hemisphere multiplicities are expected to decrease with p_{\perp} owing to the reduction of available energy, while away-hemisphere multiplicities may increase if the C -component multiplicities rise sufficiently rapidly. The predictions for toward-hemisphere multiplicities are shown in Fig. 14. They are obtained by interpolating the *observed* low- p_{\perp} hemisphere multiplicities measured in this experiment at all five ISR energies, using the expression for \sqrt{s}_R above. The shaded band represents the range of possible predictions arising from different methods of estimating the factor $\langle 1/\sin\theta \rangle_C$. The predictions reproduce the toward-hemisphere multiplicities in a qualitative way at the middle ISR energy; however, they overestimate the observed values at higher \sqrt{s} .¹¹ This lack of agreement indicates a failure of the simplified picture presented above. These quantitative deviations can be due to differences between the residual collision products at reduced energy and particles from real, low- p_{\perp} , collisions at the same lower energy. Further factors affecting these predictions include the possible production of a small fraction of the C component in the toward hemisphere and the possible production of some charged particles in the B component. The predictions are sensitive to the s dependence of the inclusive cross sections. We take the results of the prediction for the toward-hemisphere multiplicities as a measure of the validity of our picture; $N^{(\text{toward})}$ is reproduced to about 10% at all \sqrt{s} and p_{\perp} .

We proceed then to extract the C -component multiplicities,

$$N_C(\sqrt{s}; p_{\perp}) = N^{(\text{away})}(\sqrt{s}; p_{\perp}) - N_A(\sqrt{s}_R; \text{low } p_{\perp}),$$

using the same low- p_{\perp} A -component hemisphere multiplicities interpolated from the data as in the toward-hemisphere case. Thus, we may determine the associated multiplicity of the C component at various energies vs p_{\perp} . The results are shown in Fig. 15. We note the striking result that the C multiplicity thus obtained is, within the uncertainties of this analysis, linearly dependent on p_{\perp} and is *independent of energy*. The slope of the p_{\perp} dependence is about $\frac{2}{3}$ charged particles/(GeV/c).

We point out that the average p_{\perp} of these C particles (assuming that there are an equal number of π^+ , π^- , and π^0 produced, all with the same average p_{\perp}) is ~ 1 GeV/c, which is about three times the average value in inclusive events.

Encouraged by the energy independence of the C multiplicity, we study its angular distribution. That is, we compute

$$\frac{dN_C}{d\eta}(\sqrt{s}, \eta; p_{\perp}) = \frac{dN^{(\text{away})}}{d\eta}(\sqrt{s}, \eta; p_{\perp}) - \frac{dN_A}{d\eta}(\sqrt{s}_R, \eta; \text{low } p_{\perp}).$$

The angular distribution of the C component calculated in this way is shown in Fig. 16 for the

TABLE VII. Differential multiplicity distributions for away and toward hemispheres. Photon detector is at 8° , and $\sqrt{s} = 23$ GeV.

Away hemisphere $dN/d\eta$				
η	p_{\perp} (GeV/c) 0.0-0.5	p_{\perp} (GeV/c) 0.5-1.0	p_{\perp} (GeV/c) 1.0-1.5	p_{\perp} (GeV/c) 1.5-2.0
-4.74	0.087 ± 0.002	0.095 ± 0.003	0.077 ± 0.004	0.061 ± 0.027
-4.20	0.174 ± 0.002	0.199 ± 0.003	0.184 ± 0.006	0.242 ± 0.073
-3.65	0.354 ± 0.005	0.421 ± 0.008	0.391 ± 0.013	0.332 ± 0.114
-3.19	0.660 ± 0.007	0.732 ± 0.011	0.801 ± 0.021	0.933 ± 0.216
-2.79	0.867 ± 0.009	0.916 ± 0.013	1.048 ± 0.026	0.865 ± 0.193
-2.46	1.047 ± 0.010	1.097 ± 0.015	1.174 ± 0.029	1.134 ± 0.245
-2.19	1.225 ± 0.012	1.235 ± 0.017	1.339 ± 0.032	1.296 ± 0.271
-1.95	1.334 ± 0.013	1.308 ± 0.017	1.463 ± 0.035	1.710 ± 0.379
-1.76	1.423 ± 0.014	1.397 ± 0.019	1.573 ± 0.038	2.268 ± 0.431
-1.60	1.349 ± 0.013	1.427 ± 0.020	1.610 ± 0.040	1.412 ± 0.345
-1.46	1.392 ± 0.014	1.444 ± 0.021	1.616 ± 0.041	1.569 ± 0.342
-1.34	1.463 ± 0.015	1.433 ± 0.021	1.640 ± 0.043	1.708 ± 0.352
-0.92	1.490 ± 0.012	1.463 ± 0.017	1.643 ± 0.033	1.872 ± 0.321
-0.65	1.470 ± 0.012	1.466 ± 0.016	1.591 ± 0.032	1.901 ± 0.354
-0.34	1.450 ± 0.011	1.395 ± 0.015	1.611 ± 0.032	1.691 ± 0.306
0.00	1.475 ± 0.012	1.412 ± 0.016	1.535 ± 0.031	1.516 ± 0.266
0.34	1.495 ± 0.012	1.413 ± 0.016	1.558 ± 0.031	2.320 ± 0.362
0.65	1.558 ± 0.013	1.419 ± 0.016	1.600 ± 0.033	1.828 ± 0.317
0.92	1.613 ± 0.013	1.448 ± 0.016	1.536 ± 0.031	1.832 ± 0.377
1.34	1.726 ± 0.018	1.403 ± 0.021	1.553 ± 0.041	1.251 ± 0.336
1.46	1.755 ± 0.018	1.433 ± 0.020	1.505 ± 0.038	0.899 ± 0.255
1.60	1.750 ± 0.018	1.387 ± 0.021	1.386 ± 0.036	1.221 ± 0.305
1.76	1.733 ± 0.017	1.402 ± 0.019	1.312 ± 0.033	1.514 ± 0.354
1.95	1.676 ± 0.016	1.338 ± 0.018	1.156 ± 0.030	0.813 ± 0.245
2.19	1.549 ± 0.016	1.249 ± 0.018	0.993 ± 0.029	0.739 ± 0.230
2.46	1.367 ± 0.016	1.131 ± 0.018	0.803 ± 0.028	0.714 ± 0.235
2.79	1.149 ± 0.014	0.926 ± 0.016	0.549 ± 0.023	0.171 ± 0.164
3.19	0.799 ± 0.011	0.543 ± 0.011	0.189 ± 0.014	0.013 ± 0.099
3.65	0.323 ± 0.005	0.172 ± 0.005	0.042 ± 0.006	0.055 ± 0.061
4.20	0.142 ± 0.002	0.091 ± 0.002	0.047 ± 0.003	0.033 ± 0.015
4.74	0.058 ± 0.001	0.032 ± 0.001	0.020 ± 0.002	0.001 ± 0.000
Toward hemisphere $dN/d\eta$				
η	p_{\perp} (GeV/c) 0.0-0.5	p_{\perp} (GeV/c) 0.5-1.0	p_{\perp} (GeV/c) 1.0-1.5	p_{\perp} (GeV/c) 1.5-2.0
-4.74	0.087 ± 0.002	0.082 ± 0.002	0.074 ± 0.004	0.039 ± 0.027
-4.20	0.174 ± 0.002	0.168 ± 0.003	0.144 ± 0.005	0.144 ± 0.047
-3.65	0.354 ± 0.004	0.343 ± 0.006	0.339 ± 0.011	0.576 ± 0.136
-3.19	0.660 ± 0.007	0.632 ± 0.009	0.629 ± 0.016	0.510 ± 0.135
-2.79	0.867 ± 0.008	0.823 ± 0.011	0.814 ± 0.020	0.809 ± 0.179
-2.46	1.047 ± 0.010	1.003 ± 0.014	1.000 ± 0.025	0.966 ± 0.220
-2.19	1.225 ± 0.012	1.097 ± 0.015	1.121 ± 0.028	0.908 ± 0.229
-1.95	1.334 ± 0.013	1.182 ± 0.017	1.176 ± 0.031	0.737 ± 0.222
-1.76	1.423 ± 0.014	1.267 ± 0.018	1.273 ± 0.033	0.504 ± 0.180
-1.60	1.349 ± 0.013	1.271 ± 0.019	1.244 ± 0.034	1.027 ± 0.238
-1.46	1.392 ± 0.013	1.286 ± 0.020	1.299 ± 0.039	0.850 ± 0.244
-1.34	1.463 ± 0.017	1.300 ± 0.021	1.244 ± 0.039	1.020 ± 0.344
-0.92	1.490 ± 0.016	1.231 ± 0.020	1.166 ± 0.037	1.691 ± 0.406
-0.65	1.470 ± 0.016	1.139 ± 0.018	1.127 ± 0.034	1.190 ± 0.373
-0.34	1.450 ± 0.015	1.093 ± 0.017	1.054 ± 0.032	1.119 ± 0.298
0.00	1.475 ± 0.015	1.085 ± 0.017	1.015 ± 0.031	1.201 ± 0.329
0.34	1.495 ± 0.015	1.044 ± 0.017	0.958 ± 0.031	1.255 ± 0.363
0.65	1.558 ± 0.017	1.018 ± 0.017	0.910 ± 0.030	0.618 ± 0.252
0.92	1.613 ± 0.018	0.990 ± 0.018	0.822 ± 0.031	0.784 ± 0.265
1.34	1.726 ± 0.020	1.109 ± 0.020	0.909 ± 0.033	0.857 ± 0.308
1.46	1.755 ± 0.019	1.096 ± 0.019	0.853 ± 0.032	0.901 ± 0.302
1.60	1.750 ± 0.018	1.171 ± 0.018	0.886 ± 0.028	0.829 ± 0.257
1.76	1.733 ± 0.017	1.151 ± 0.017	0.842 ± 0.028	0.649 ± 0.199
1.95	1.676 ± 0.016	1.091 ± 0.016	0.819 ± 0.027	1.028 ± 0.274
2.19	1.549 ± 0.014	1.057 ± 0.015	0.744 ± 0.022	0.408 ± 0.141
2.46	1.367 ± 0.012	0.961 ± 0.012	0.704 ± 0.018	0.762 ± 0.180
2.79	1.149 ± 0.010	0.780 ± 0.009	0.593 ± 0.013	0.413 ± 0.075
3.19	0.799 ± 0.007	0.522 ± 0.007	0.364 ± 0.009	0.421 ± 0.089
3.65	0.323 ± 0.003	0.183 ± 0.003	0.115 ± 0.005	0.160 ± 0.046
4.20	0.142 ± 0.002	0.085 ± 0.002	0.052 ± 0.003	0.103 ± 0.051
4.74	0.058 ± 0.001	0.032 ± 0.001	0.024 ± 0.002	0.018 ± 0.017

data taken at $\sqrt{s} = 53$ GeV. The angular distribution, although narrower than the angular distribution seen in average inelastic collisions, is none-the less quite broad. The width of the C -component angular distribution is about 80% of the width of the angular distribution observed when a low- p_{\perp} particle is detected at $\theta = 90^{\circ}$.

We have studied the variations in the width in η for the C -component distributions. We compute at each \sqrt{s} and p_{\perp} the mean dispersion $\langle \eta^2 \rangle^{1/2}$ for the C distributions shown in Fig. 16. These dispersions are plotted in Fig. 17 for all ISR energies as a function of p_{\perp} . Although the errors are large, the trend seems to be that the C dispersion decreases slowly with increasing p_{\perp} . There is an indication that the C dispersion tends to increase with increasing \sqrt{s} , although such an effect is not

clearly established.

We conclude that the data support the phenomenological picture that production of particles in large- p_{\perp} events may be considered a superposition of the B and C components, containing the large- p_{\perp} particles, and the A component resembling ordinary, low- p_{\perp} collision products. In this picture, the C component, which balances the transverse momentum of the trigger, has a multiplicity which depends *only* upon the value of p_{\perp} . The width of the C component in η decreases slowly as p_{\perp} is increased.

VI. COMPARISON WITH MODELS

Several models have been developed which deal with particle production at large p_{\perp} in hadronic

TABLE VIII. Differential multiplicity distributions for away and toward hemispheres. Photon detector is at 8° , and $\sqrt{s} = 53$ GeV.

Away hemisphere $dN/d\eta$						
η	p_{\perp} (GeV/c) 0.0-0.5	p_{\perp} (GeV/c) 0.5-1.0	p_{\perp} (GeV/c) 1.0-1.5	p_{\perp} (GeV/c) 1.5-2.0	p_{\perp} (GeV/c) 2.0-2.5	p_{\perp} (GeV/c) 2.5-3.0
-4.74	0.224 ± 0.004	0.236 ± 0.005	0.223 ± 0.014	0.206 ± 0.013	0.190 ± 0.008	0.175 ± 0.027
-4.20	0.475 ± 0.006	0.485 ± 0.008	0.494 ± 0.022	0.476 ± 0.021	0.476 ± 0.014	0.415 ± 0.047
-3.65	0.775 ± 0.011	0.788 ± 0.014	0.866 ± 0.040	0.903 ± 0.040	0.877 ± 0.026	0.842 ± 0.091
-3.19	1.022 ± 0.011	1.049 ± 0.015	1.106 ± 0.043	1.150 ± 0.042	1.286 ± 0.031	1.442 ± 0.116
-2.77	1.251 ± 0.014	1.288 ± 0.018	1.397 ± 0.051	1.464 ± 0.052	1.579 ± 0.037	1.567 ± 0.133
-2.46	1.407 ± 0.015	1.469 ± 0.020	1.570 ± 0.059	1.666 ± 0.059	1.778 ± 0.041	2.145 ± 0.165
-2.19	1.492 ± 0.016	1.534 ± 0.021	1.596 ± 0.060	1.741 ± 0.061	1.921 ± 0.045	2.137 ± 0.161
-1.95	1.526 ± 0.016	1.541 ± 0.021	1.746 ± 0.064	1.726 ± 0.060	1.993 ± 0.045	2.159 ± 0.172
-1.76	1.570 ± 0.018	1.597 ± 0.023	1.723 ± 0.066	1.876 ± 0.068	2.003 ± 0.047	2.642 ± 0.216
-1.60	1.588 ± 0.019	1.617 ± 0.024	1.752 ± 0.068	1.859 ± 0.068	2.037 ± 0.049	2.627 ± 0.205
-1.46	1.585 ± 0.019	1.600 ± 0.025	1.684 ± 0.071	1.844 ± 0.071	2.007 ± 0.050	2.371 ± 0.202
-1.34	1.563 ± 0.019	1.594 ± 0.025	1.743 ± 0.072	1.930 ± 0.072	2.065 ± 0.053	2.326 ± 0.215
-0.92	1.556 ± 0.015	1.571 ± 0.019	1.772 ± 0.058	1.890 ± 0.059	2.097 ± 0.044	2.282 ± 0.167
-0.65	1.528 ± 0.015	1.546 ± 0.019	1.618 ± 0.054	1.840 ± 0.057	2.117 ± 0.043	2.399 ± 0.167
-0.34	1.502 ± 0.015	1.551 ± 0.019	1.587 ± 0.053	1.921 ± 0.059	2.099 ± 0.043	2.550 ± 0.174
0.00	1.546 ± 0.015	1.566 ± 0.019	1.741 ± 0.058	1.819 ± 0.057	2.104 ± 0.043	2.409 ± 0.173
0.34	1.589 ± 0.015	1.585 ± 0.019	1.755 ± 0.057	1.893 ± 0.059	2.120 ± 0.043	2.391 ± 0.178
0.65	1.640 ± 0.016	1.647 ± 0.020	1.803 ± 0.059	2.030 ± 0.061	2.169 ± 0.044	2.085 ± 0.146
0.92	1.769 ± 0.017	1.737 ± 0.021	1.884 ± 0.061	2.162 ± 0.066	2.319 ± 0.047	2.214 ± 0.163
1.34	1.904 ± 0.024	1.818 ± 0.029	1.901 ± 0.080	2.074 ± 0.082	2.218 ± 0.058	1.963 ± 0.191
1.46	1.997 ± 0.024	1.875 ± 0.028	1.922 ± 0.077	2.133 ± 0.079	2.268 ± 0.056	2.220 ± 0.202
1.60	2.052 ± 0.024	1.926 ± 0.029	1.932 ± 0.076	2.210 ± 0.079	2.238 ± 0.055	1.939 ± 0.180
1.76	2.112 ± 0.024	1.986 ± 0.029	2.043 ± 0.078	2.231 ± 0.076	2.188 ± 0.053	1.817 ± 0.167
1.95	2.157 ± 0.025	2.060 ± 0.029	1.970 ± 0.074	2.031 ± 0.073	2.143 ± 0.052	2.072 ± 0.186
2.19	2.228 ± 0.027	2.098 ± 0.032	2.082 ± 0.084	1.933 ± 0.077	1.952 ± 0.052	1.758 ± 0.180
2.46	2.180 ± 0.030	2.020 ± 0.034	2.122 ± 0.092	1.627 ± 0.076	1.451 ± 0.049	1.152 ± 0.157
2.77	1.989 ± 0.028	1.836 ± 0.032	1.631 ± 0.079	1.356 ± 0.070	0.967 ± 0.041	0.620 ± 0.125
3.19	1.574 ± 0.023	1.417 ± 0.026	1.165 ± 0.063	0.820 ± 0.052	0.614 ± 0.031	0.348 ± 0.100
3.65	1.061 ± 0.015	0.953 ± 0.018	0.815 ± 0.043	0.550 ± 0.035	0.332 ± 0.018	0.160 ± 0.047
4.20	0.549 ± 0.006	0.498 ± 0.007	0.383 ± 0.017	0.312 ± 0.015	0.219 ± 0.008	0.176 ± 0.025
4.74	0.181 ± 0.003	0.151 ± 0.004	0.106 ± 0.009	0.088 ± 0.008	0.054 ± 0.004	0.047 ± 0.014
Toward hemisphere $dN/d\eta$						
-4.74	0.224 ± 0.004	0.221 ± 0.005	0.204 ± 0.014	0.210 ± 0.013	0.182 ± 0.008	0.155 ± 0.026
-4.20	0.475 ± 0.006	0.463 ± 0.007	0.477 ± 0.021	0.438 ± 0.019	0.407 ± 0.012	0.363 ± 0.044
-3.65	0.775 ± 0.010	0.747 ± 0.012	0.687 ± 0.032	0.790 ± 0.033	0.733 ± 0.022	0.692 ± 0.080
-3.19	1.022 ± 0.010	1.000 ± 0.013	0.981 ± 0.036	1.042 ± 0.036	0.987 ± 0.023	1.054 ± 0.089
-2.77	1.251 ± 0.013	1.229 ± 0.016	1.245 ± 0.045	1.217 ± 0.042	1.298 ± 0.030	1.317 ± 0.108
-2.46	1.407 ± 0.015	1.366 ± 0.019	1.380 ± 0.052	1.538 ± 0.054	1.444 ± 0.035	1.321 ± 0.120
-2.19	1.492 ± 0.017	1.424 ± 0.020	1.497 ± 0.058	1.443 ± 0.054	1.548 ± 0.039	1.634 ± 0.146
-1.95	1.526 ± 0.018	1.479 ± 0.022	1.457 ± 0.060	1.543 ± 0.060	1.608 ± 0.042	1.795 ± 0.155
-1.76	1.570 ± 0.018	1.534 ± 0.023	1.629 ± 0.065	1.576 ± 0.061	1.648 ± 0.042	1.921 ± 0.163
-1.60	1.588 ± 0.019	1.507 ± 0.024	1.517 ± 0.065	1.499 ± 0.063	1.597 ± 0.043	1.888 ± 0.180
-1.46	1.585 ± 0.021	1.506 ± 0.025	1.439 ± 0.068	1.673 ± 0.071	1.698 ± 0.049	1.773 ± 0.174
-1.34	1.563 ± 0.021	1.490 ± 0.026	1.412 ± 0.069	1.691 ± 0.074	1.669 ± 0.050	1.765 ± 0.174
-0.92	1.556 ± 0.021	1.414 ± 0.025	1.521 ± 0.070	1.664 ± 0.071	1.724 ± 0.049	1.753 ± 0.174
-0.65	1.528 ± 0.020	1.374 ± 0.024	1.416 ± 0.066	1.558 ± 0.068	1.550 ± 0.045	1.468 ± 0.157
-0.34	1.502 ± 0.019	1.379 ± 0.023	1.463 ± 0.066	1.520 ± 0.064	1.546 ± 0.044	1.478 ± 0.157
0.00	1.546 ± 0.020	1.409 ± 0.023	1.526 ± 0.067	1.478 ± 0.064	1.561 ± 0.044	1.485 ± 0.160
0.34	1.589 ± 0.021	1.388 ± 0.024	1.400 ± 0.066	1.398 ± 0.062	1.463 ± 0.043	1.524 ± 0.157
0.65	1.640 ± 0.022	1.392 ± 0.024	1.380 ± 0.067	1.389 ± 0.065	1.413 ± 0.044	1.267 ± 0.149
0.92	1.769 ± 0.024	1.475 ± 0.027	1.466 ± 0.072	1.268 ± 0.066	1.444 ± 0.047	1.379 ± 0.171
1.34	1.904 ± 0.026	1.573 ± 0.028	1.674 ± 0.081	1.468 ± 0.072	1.502 ± 0.049	1.506 ± 0.172
1.46	1.997 ± 0.027	1.623 ± 0.029	1.509 ± 0.075	1.508 ± 0.071	1.430 ± 0.047	1.516 ± 0.176
1.60	2.052 ± 0.026	1.698 ± 0.028	1.531 ± 0.070	1.727 ± 0.073	1.435 ± 0.044	1.305 ± 0.156
1.76	2.112 ± 0.026	1.729 ± 0.028	1.550 ± 0.071	1.596 ± 0.068	1.483 ± 0.044	1.418 ± 0.153
1.95	2.157 ± 0.026	1.884 ± 0.029	1.744 ± 0.074	1.589 ± 0.069	1.498 ± 0.044	1.531 ± 0.164
2.19	2.228 ± 0.025	1.941 ± 0.028	1.749 ± 0.069	1.581 ± 0.060	1.561 ± 0.041	1.737 ± 0.153
2.46	2.180 ± 0.023	1.951 ± 0.025	1.672 ± 0.059	1.522 ± 0.053	1.502 ± 0.036	1.245 ± 0.110
2.77	1.989 ± 0.019	1.708 ± 0.020	1.594 ± 0.050	1.418 ± 0.044	1.205 ± 0.025	1.146 ± 0.086
3.19	1.574 ± 0.015	1.325 ± 0.016	1.175 ± 0.037	1.054 ± 0.033	0.868 ± 0.018	0.653 ± 0.065
3.65	1.061 ± 0.013	0.826 ± 0.013	0.840 ± 0.031	0.548 ± 0.027	0.420 ± 0.015	0.341 ± 0.047
4.20	0.549 ± 0.007	0.428 ± 0.007	0.312 ± 0.016	0.258 ± 0.015	0.204 ± 0.009	0.205 ± 0.035
4.74	0.181 ± 0.003	0.130 ± 0.003	0.104 ± 0.008	0.084 ± 0.007	0.064 ± 0.004	0.041 ± 0.012

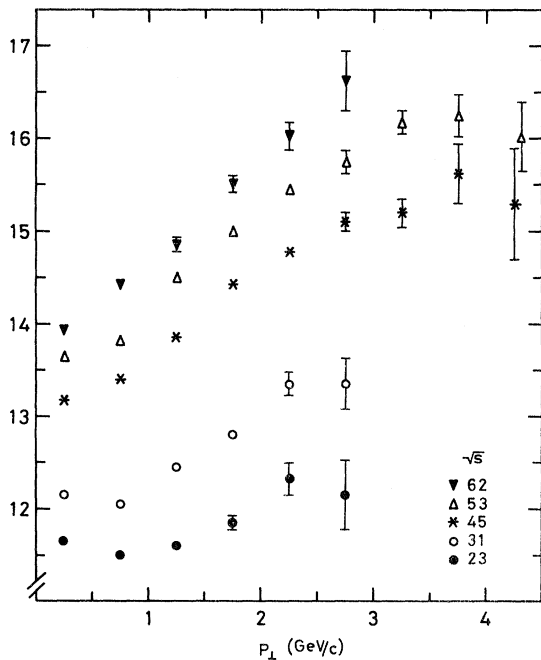


FIG. 12. Total unnormalized charged multiplicities as a function of p_{\perp} of the photon for several values of \sqrt{s} (in GeV).

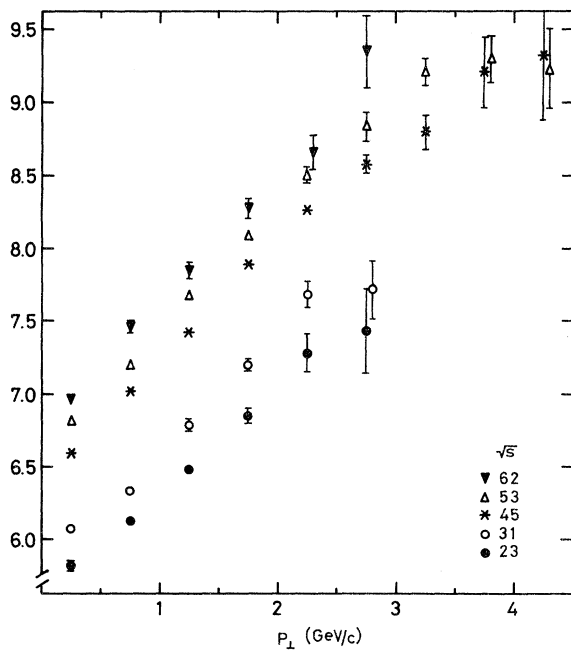


FIG. 13. Unnormalized multiplicities of charged particles in the hemisphere away from the photon in azimuth (rapidity ≈ 0) versus p_{\perp} for several values of \sqrt{s} (in GeV).

collisions. The original motivation for these studies was the explanation of the p_{\perp} and s dependences of inclusive cross sections. It is, therefore, of considerable interest to confront such models with the data concerning the structure of events containing a large- p_{\perp} secondary, with the aim of sharpening our understanding of the dynamical mechanisms involved. Since these models have not, in general, been applied in detail to the question of event structure, our comments will be based primarily on their qualitative aspects.

The comments on this section should, of course, be regarded as independent of the experimental findings of the preceding sections. They are included here as representative of our opinions regarding the dynamical origin of large- p_{\perp} phenomena. However, we recognize that most models retain sufficient freedom to evolve toward a description of the available data. A discussion of the models and references to the literature can be found in the summary by Ellis¹² and the review of Sivvers, Brodsky, and Blankenbecler.²

We begin with a summary of the experimental data from this and other experiments on the composition of events containing large- p_{\perp} particles:

(i) Associated multiplicities in the hemisphere away from the triggering particle increase with

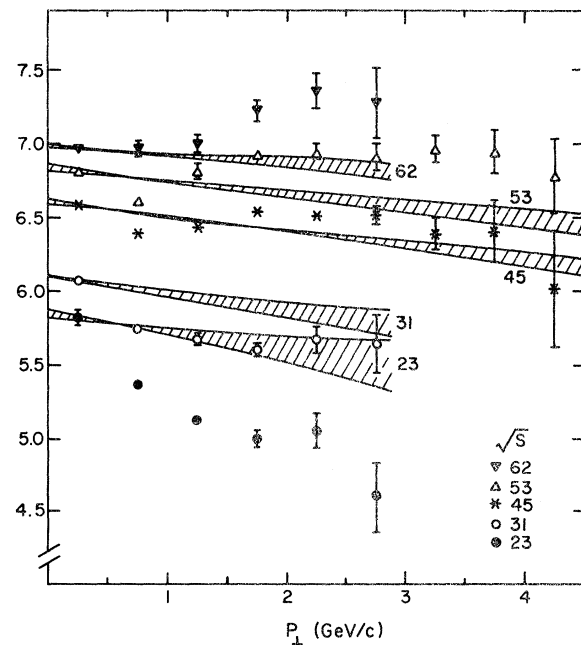


FIG. 14. Unnormalized multiplicities of charged particles in the hemisphere toward the photon (rapidity ≈ 0) versus p_{\perp} for several values of \sqrt{s} (in GeV). The shaded regions represent the range of predictions of the phenomenological picture discussed in Sec. V.

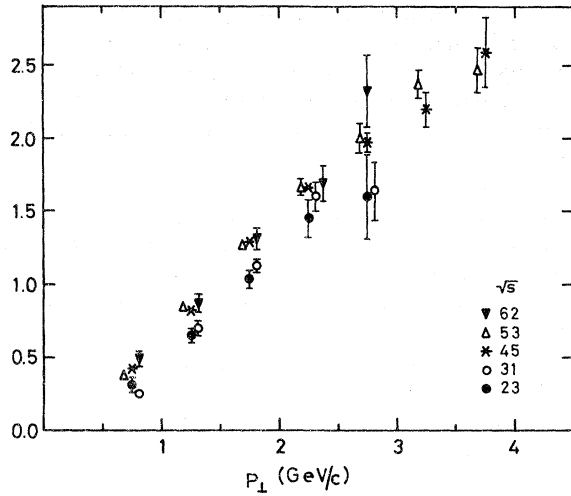


FIG. 15. Unnormalized multiplicity of the C component (discussed in Sec. V) versus p_{\perp} at various values of \sqrt{s} (in GeV). Photon rapidity ≈ 0 .

increasing p_{\perp} (Fig. 13).

(ii) Associated multiplicities in the toward hemisphere decrease with increasing p_{\perp} at all but the highest ISR energies, where they are approximately constant (Fig. 14).

(iii) The angular extent of the multiplicity excess is large. It covers approximately ± 2 units in rapidity (Fig. 9) and $\pm 60^\circ$ in the azimuthal region (Figs. 10 and 11). The angular size of the excess is nearly independent of p_{\perp} and s (Fig. 17).

(iv) When the trigger particle is not at 90° , the multiplicity excess is largest in the polar-angle hemisphere *away from* the trigger particle (Fig.

9). This “back-to-back” configuration is not fully developed as the excess multiplicity lies between the backward extension of the trigger axis (\hat{E}) and $\theta = 90^\circ$.¹³

(v) The existence of a large- p_{\perp} particle implies that those particles observed in the opposite hemisphere have a mean transverse momentum of about 1 GeV/c (Fig. 15), independent of p_{\perp} and s . This result is seen clearly, in a limited angular range, by experiments which measure the momenta of the particles opposite the trigger.¹⁴ (These experiments also show that the presence of a large- p_{\perp} trigger particle *enhances* the probability for finding a large- p_{\perp} particle alongside the trigger.)

(vi) Recent studies¹⁵ in which particle momenta are measured show important scaling properties among the particles which balance the p_{\perp} of the trigger. In particular, they observe that for these particles, the component of momentum perpendicular to the trigger plane (p_{out}) is limited ($p_{out} \lesssim 0.4$ GeV/c), and has a distribution which is independent of p_{\perp} or the angle of emission of the triggering secondary. They also observe that the distribution of events in the quantity $x_B = (\vec{p} \cdot \hat{E})/p_{\perp}$ is independent of the p_{\perp} of the trigger particle.

A. Fireball models

The central idea of these models is that the incident energy is converted to one or several massive “fireball” states. It is assumed that the fireballs are produced with low p_{\perp} , and subsequently decay isotropically to the observed hadrons. The

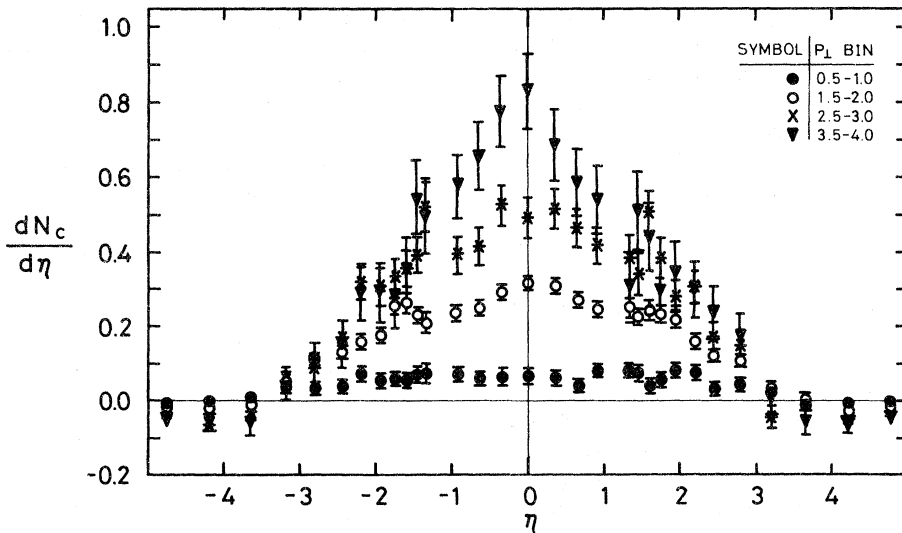


FIG. 16. Unnormalized multiplicity distribution of the C component (discussed in Sec. V) versus η for several values of p_{\perp} (in GeV/c). These data are for $\sqrt{s} = 53$ GeV and photon rapidity ≈ 0 .

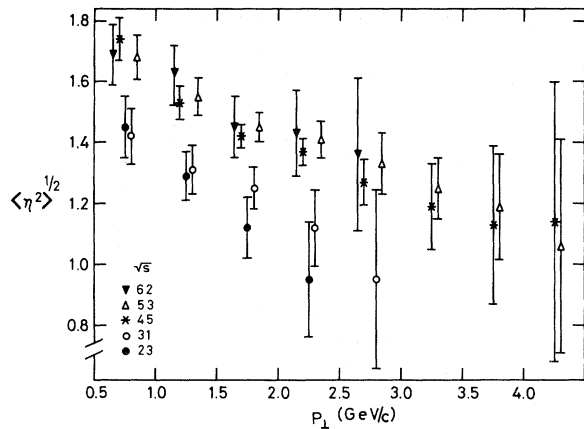


FIG. 17. Dispersion $\langle \eta^2 \rangle^{1/2}$ of the C component (discussed in Sec. V) versus p_{\perp} at several values of \sqrt{s} (photon rapidity ≈ 0).

number and mass spectrum of the fireballs varies from model to model; we discuss several possibilities below.

The oldest and simplest fireball picture¹⁶ assumes a single massive state at rest in the c.m. with $M = \sqrt{s}/c^2$. Given such a restrictive (fixed-mass) picture, it is difficult to reproduce the overall increase in multiplicity with p_{\perp} . Moreover, with such a heavy fireball ($M \sim 30 \text{ GeV}/c^2$) and $p_{\perp} < 5 \text{ GeV}/c$ it is difficult to produce the localization of particles observed [point (iii) above]. If one relaxes the requirement that this single stationary fireball contains the full c.m. energy, it becomes possible to reproduce the observed angular widths of the multiplicity access by requiring that a trigger particle of momentum p originate from a fireball of mass $M \approx (2 - 3)p/c$. The growth in associated multiplicity [point (i)] then has a natural explanation, if one assumes a proportionality between the fireball mass and its decay multiplicity. However, for a stationary fireball the region of maximum multiplicity increase would be expected directly opposite to the trigger particle, in disagreement with the data [point (iv)].

The production of several fireballs offers some additional degrees of freedom with which to fit the data. Several possibilities can be explored for the fireball mass spectrum; heavy fireballs ($M \gtrsim 5 \text{ GeV}/c^2$) may be postulated,¹⁷ or one can imagine the fireballs to be the high-mass tail of the clusters introduced to explain low- p_{\perp} correlation data.¹⁸ By allowing the fireballs to have a longitudinal momentum distribution, and by retaining the proportionality between fireball mass and observed trigger momentum, we find that the qualitative

aspects of the associated multiplicity distributions [points (i) and (iv)] can be reproduced. The fireball masses required are $\gtrsim 10 \text{ GeV}/c^2$ for trigger photons of $p_{\perp} = 3 \text{ GeV}/c$ in order that some tendency toward back-to-back structure be observed for $\theta \neq 90^\circ$.

The fireball models, in any of the forms outlined above, have no natural mechanism for explaining the momentum correlations [points (v) and (vi)]. In particular, we find it difficult to understand the tendency for positive alongside momentum correlations of the strength observed.¹⁴ In addition, the fireball masses required seem rather large, compared with the usual mass scale of hadronic systems.

B. Bremsstrahlung models

It has been proposed¹⁹ that particle production at large p_{\perp} is dominated by a bremsstrahlung process by which neutral vector mesons are radiated from the colliding hadrons. These ρ^0, ω, \dots then decay to give the observed particles. Such a model can give a reasonable power-law behavior for the inclusive cross section and can reproduce the global multiplicity increase as a function of p_{\perp} .

Detailed calculations of correlations are lacking within this model; however, we find it difficult to reconcile the data with a picture in which low-mass states give rise to the large- p_{\perp} particle for reasons rather similar to those discussed in connection with low-mass fireballs above. In particular, we do not see natural explanations for the increased momentum of recoiling particles [point (v)] or for the tendency toward back-to-back production of trigger and recoils [point (iv)]. It might be supposed that the alongside momentum correlations [point (v)] could be expected in a model in which the large- p_{\perp} trigger is the result of a vector-meson decay. In such a case, the other decay product(s) will tend to share the original meson's transverse momentum. However, recent detailed studies²⁰ of this mechanism show that resonance decay is, in fact, quite insufficient to reproduce these same-side correlations. A further prediction of bremsstrahlung models, concerning the absence of leading particles in large- p_{\perp} events, is in contradiction with a recent experiment.²¹

C. Hard-scattering models

Extensive studies¹² have been made of large- p_{\perp} hadron collisions within the framework of parton, or hard-scattering, models. Details vary considerably, but the essential features are that (i)

constituents within the colliding hadrons (partons or other hadrons) undergo a single large-momentum-transfer collision, (ii) the amplitude for the hard scatter is a power-law function of momentum transfer, and (iii) the scattered constituents are modified through final-state interactions to give "jets" of observed particles centered on the scattered constituent directions. The jets can be single particles or resonances or several particles shaken off the scattered constituent during its exit from the interaction volume. Since the basic process is a two-particle interaction, this model introduces a natural plane of symmetry containing the incident hadrons and the large- p_{\perp} trigger particle.

Although rather large degrees of freedom exists within these models (e.g., the nature of the scattering constituents and their amplitudes), the experimental observations enumerated above have quite natural and qualitative explanations. The multiplicity increase in the away hemisphere results from the basic features of the jet. The original scattered constituent gives rise to a series of particles which share the original momentum and have typically low-momentum components perpendicular to the scattered constituent direction. The jet development is conceived to be similar to production of low-transverse-momentum particles in typical hadronic collisions. The number of particles in the jet thus depends on the energy of the original constituent, consistent with the data [point (i)]. The jet which gives rise to the trigger particle is highly biased by the requirement that the trigger have large p_{\perp} ; the resulting alongside jet is, thus, forced to have rather low multiplicity [point (ii)].²⁰ The angular size of the recoiling jet [point (iii)] is determined by the distribution of particle momentum components along the jet axis and the sharply cut off perpendicular components. The extent of the jet in η is broadened by the distribution of longitudinal momentum components of the constituents before scattering; explicit calculations¹² show reasonable agreement with the data. Our estimates of the azimuthal extent of the multiplicity increase predicted in hard-scattering models agree reasonably well with the observed values. The fact that the azimuthal size is approximately independent of p_{\perp} arises, in these models, through the assumption that the particles in the jet are distributed uniformly in y_E (the rapidity along the jet axis \hat{E}) with a cutoff in the momentum components perpendicular to \hat{E} . As p_{\perp} increases, the reduced azimuthal angle ϕ of the large- y_E particles is approximately compensated by the large ϕ of those new particles introduced at low y_E . The back-to-back correlation [point (iv)] is most natural in parton pictures owing to the

basic two-body scattering process. Lack of full back-to-back structure can be understood in terms of the distribution of the initial longitudinal momenta of the constituents.¹² The expectation within parton-jet models for momentum correlations [points (v) and (vi)] has been studied in some detail²⁰ and has been found to be in satisfactory agreement with the data.

The known features of the structure of large- p_{\perp} events all have some reasonable explanation within the constituent models. However, it is well to remember that, at present, no single version of the model has successfully described these features together with the data on single-particle production cross sections and particle ratios. The connection with inelastic electroproduction data and the elucidation of the dominant constituent scattering amplitudes remains vague.

D. Summary

We find that the observed properties of events containing a large- p_{\perp} trigger particle can be understood rather naturally, in a qualitative sense, within the framework of hard-scattering models. The alternative pictures of fireball production or hadronic bremsstrahlung are not directly motivated by an underlying picture of hadronic interactions; they are usually constructed in order to reproduce the general features of the data themselves. They have not been fully developed on the question of correlations in large- p_{\perp} events. It is our opinion that these pictures are somewhat strained by the data presently available. However, they also possess sufficient flexibility that it seems difficult to reject them totally on an objective basis. We may hope that new experiments providing more detailed information (e.g., momentum correlations and particle identification over the full solid angle, and individual event configurations), especially at very large p_{\perp} , will enlighten us as to the effects of the large- p_{\perp} dynamics, and that, armed with this knowledge, we may be able to frame more detailed and more accurate models.

ACKNOWLEDGMENTS

We have enjoyed the warm hospitality and support of CERN during the course of the experiment. In particular, we are grateful to the ISR staff for the excellent performance and improvement of the machine. We thank especially J. Renaud for his efforts during the installation of the apparatus. We have also benefited from any technical dis-

cussions with the members of the CERN-Columbia-Rockefeller Collaboration. We thank G. Abshire and J. Crouch for their assistance in the data taking. A Bechini, M. Favati, and P. Marchi

have contributed with skill and enthusiasm to the construction of the detectors and electronics. We appreciate the assistance of K. M. Kephart during the lead-glass calibration measurement.

*Work supported in part by the National Science Foundation and by the Consiglio Nazionale delle Ricerche of Italy.

†Present address: Carnegie—Mellon University, Pittsburgh, Pennsylvania.

‡Present address: University of Michigan, Ann Arbor, Michigan.

§Also at Laboratori Nazionali del CNEN, Frascati, Italy.

||Also CERN Fellow.

¹F. W. Büsser *et al.*, Phys. Lett. **46B**, 471 (1973). For more recent information on single-particle inclusive cross sections see *Proceedings of the XVII International Conference on High Energy Physics, London, 1974*, edited by J. R. Smith (Rutherford Laboratory, Chilton, Didcot, Berkshire, England, 1974), in particular the contributions of G. Jarlskog and H. Frisch (see pp. V-3 and V-8).

²A review of constituent models and large- p_{\perp} phenomena is given by P. V. Landshoff, in *Proceedings of the XVII International Conference on High Energy Physics, London, 1974*, edited by J. R. Smith (Rutherford Laboratory, Chilton, Didcot, Berkshire, England, 1974), p. V-57. See also D. Sivers, S. J. Brodsky, and R. Blankenbecler, Phys. Rep. **23C**, 1 (1976) and P. Darriulat, Phys. Rep. (to be published).

³G. Finocchiaro *et al.*, Phys. Lett. **50B**, 396 (1974).

⁴These results are summarized by L. di Lella, in *Proceedings of the XVII International Conference on High Energy Physics, London, 1974*, edited by J. R. Smith (Rutherford Laboratory, Chilton, Didcot, Berkshire, England, 1974), p. V-13.

⁵P. Darriulat reviews many experimental results relating to the structure in large- p_{\perp} events, in *High Energy Physics*, proceedings of the European Physical Society International Conference, Palermo, 1975, edited by A. Zichichi (Editrice Compositori, Bologna, Italy, 1976), p. 840.

⁶An expanded account of the procedures and analysis of this experiment, together with a more complete tabulation of the data, can be found in the thesis of R. D. Kephart, State University of New York, Stony Brook, 1975 (unpublished).

⁷S. R. Amendolia *et al.*, Phys. Lett. **44B**, 119 (1973); S. R. Amendolia *et al.*, Nuovo Cimento **17A**, 735 (1973).

⁸The two-photon character of events with a neutral trigger and minimum energy deposit in a lead-glass system has been established by F. W. Büsser *et al.* (Ref. 1). In that experiment, the invariant cross sections for π^0 production were determined using two methods. The first required that a photon convert in a 0.3 radiation length lead sheet before the lead-glass array. The second method required only a minimum energy deposit in the lead-glass array. Comparison of the two methods showed that the majority of events were such that two photons were present, indicating the dominance of π^0 (or η) as the photon sources. We have reached a similar conclusion on the basis of data from this experiment by

comparing the number of elements of G_2 which were struck with the expectations based on conversion of photons from π^0 decay and shower characteristics. Similar considerations lead to the conclusion that the contamination due to \bar{n} triggers or events in which an \bar{n} accompanies a low-energy photon is less than 2%.

⁹S. R. Amendolia *et al.*, Phys. Lett. **48B**, 359 (1974);

S. R. Amendolia *et al.*, Nuovo Cimento **31A**, 17 (1976);

H. Dibon *et al.*, Phys. Lett. **44B**, 313 (1973).

¹⁰The literature of inclusive reactions is extensive.

Reviews with compilations of data and references include the following: H. Bøggild and T. Ferbel, Ann. Rev. Nucl. Sci. **24**, 451 (1974); P. Capiluppi *et al.*, Nucl. Phys. **B70**, 1 (1974); P. Capiluppi *et al.*, *ibid.* **B79**, 189 (1974); D. R. O. Morrison, CERN Report No. 73-43 (unpublished); J. Whitmore, Phys. Rep. **10C**, 273 (1974).

¹¹Recent results from the ISR suggest that the figures in Table II may substantially underestimate the differential cross section near $\eta=0$. B. Alper *et al.*, Nucl. Phys. **B100**, 237 (1975), indicate that the inclusive pion production cross section rises with s by ~ 25 – 30% over the ISR energy range. More recently, the British-CERN-MIT-Scandinavian collaboration have measured the inclusive production cross section for low-momentum charged pions at $y \approx 0$ at the ISR. Their results [K. Guettler *et al.*, Phys. Lett. **64B**, 111 (1976)] show a 36% (41%) rise in $(1/\sigma)d\sigma/dy$ for π^+ (π^-) at $y \approx 0$ over the ISR energy range. This is in marked contrast to the nearly flat s dependence of data summarized in Table II. The larger s dependence of $d\sigma/dy$ found in these experiments modifies the predicted behavior of the toward-hemisphere multiplicities discussed in Sec. V and shown in Fig. 14. The effect is to introduce a larger decrease of the expected toward-hemisphere multiplicities with increasing p_{\perp} than that derived from the data in Table II. With the new data, the prediction is reasonable at the three lowest ISR energies but falls too rapidly to agree with the higher-energy data.

¹²S. D. Ellis, in *Proceedings of the XVII International Conference on High Energy Physics, London, 1974*, edited by J. R. Smith (Rutherford Laboratory, Chilton, Didcot, Berkshire, England, 1974), p. V-23.

¹³Recent data from K. Eggert *et al.*, Nucl. Phys. **B98**, 73 (1975), with a π^0 trigger at $\theta \approx 53^\circ$ ($\eta \approx 0.75$) and $p_{\perp} \geq 3.0$ GeV/c, show that those particles whose azimuth lies within the interval $150^\circ \leq \phi \leq 210^\circ$ relative to the trigger π^0 are found preferentially near the axis \hat{E} . However this fully back-to-back component has not been observed when the trigger is a charged particle at $\theta \approx 15^\circ$ ($\eta \approx 2$) and $p_{\perp} \geq 2.5$ GeV/c (M. Della Negra *et al.*, paper submitted to the Palermo Conference, and reported in Ref. 5).

¹⁴F. W. Büsser *et al.*, Phys. Lett. **51B**, 306 (1974); **51B**, 311 (1974); F. W. Büsser *et al.*, *ibid.* **55B**, 232 (1975); K. Eggert *et al.*, Nucl. Phys. **B98**, 49 (1975).

- ¹⁵P. Darriulat *et al.*, paper submitted to the International Conference on High Energy Physics, Palermo, 1975; M. Della Negra *et al.*, paper submitted to the International Conference on High Energy Physics, Palermo, 1975.
- ¹⁶E. Fermi, Phys. Rev. 81, 683 (1951); Meng Ta-Chung, Phys. Rev. D 9, 3062 (1974).
- ¹⁷S. Sakai, Prog. Theor. Phys. 50, 1644 (1973); A. Bouquet, J. Letessier, and A. Tounsi, Phys. Lett. 51B, 235 (1974); S. Pokorski and L. Stodolsky, *ibid.* 60B, 84 (1975).
- ¹⁸J. Ranft and G. Ranft, Nucl. Phys. B53, 217 (1973); F. Hayot and A. Morel, *ibid.* B59, 493 (1973); E. L. Berger and G. C. Fox, Phys. Lett. 47B, 162 (1973).
- ¹⁹H. M. Fried, Phys. Lett. 51B, 90 (1974); A. P. Contogouris, J. P. Holden, and E. N. Argyres, *ibid.* 51B, 251 (1974).
- ²⁰S. D. Ellis, M. Jacob, and P. V. Landshoff, CERN Report No. TH2109, 1975 (unpublished).
- ²¹M. Della Negra *et al.*, Phys. Lett. 59B, 401 (1975).